Available online at www.sciencedirect.com
SCIENCE DIRECT®
Journal of Sound and Vibration 296 (2006) 417–446
JOURNAL OF SOUND AND VIBRATION
www.elsevier.com/locate/jsvi

An experimental investigation of unsteady surface pressure on an airfoil in turbulence—Part 1: Effects of mean loading

Patrick F. Mish*, William J. Devenport

Virginia Tech, Aerospace and Ocean Engineering Department, 215 Randolph Hall, Blacksburg, VA 24060, USA

Received 30 April 2003; received in revised form 6 July 2005; accepted 22 August 2005
Available online 2 May 2006

Abstract

An experimental investigation into the response of an airfoil in turbulence is undertaken and the results are presented in a two part series of papers. The effects of mean loading on the airfoil response are investigated in this paper (Part 1) with the likely sources discussed in Part 2. Unsteady surface pressure measurements were made on a NACA 0015 immersed in grid turbulence ($\lambda/c = 13\%$) for angles of attack, $\alpha = 0-20^\circ$, with a dense array of pressure transducers. These measurements reveal a reduction of up to 5 dB in pressure spectral level as the angle of attack is increased for reduced frequencies less than 5. This observed mean-loading effect has never before been measured or shown to occur theoretically. Lift spectra computed from pressure measurements show a similar result. Furthermore, the reduction in lift spectral level appears to have an α^2 dependence. Also, for small angles of attack ($\alpha < 8^\circ$) Amiet's zero-mean-loading theory may be useful for predicting the airfoil response since the reduction in spectral level is less than 1 dB here. Based on comparisons at $\alpha = 0^\circ$, Amiet's theory predicts with reasonable accuracy (within 4 dB at low frequency) pressure and lift spectral levels. This theory successfully predicts the shape of both pressure and lift spectra and the decrease in pressure spectral level moving away from the airfoil leading edge. Additionally, Reba and Kerschen's theory, which accounts for non-zero-mean loading using Rapid Distortion Theory, predicts large increases in pressure and lift spectral levels not shown to occur in the measurement. The predicted rise in spectral level appears to result from the flat-plate model with leading-edge singularity which does not fully account for the distortion of the inflow.

1. Introduction

When a lifting surface passes through turbulence pressure fluctuations are produced on its surface that can radiate broadband noise [1]. To calculate these fluctuations and thus the noise requires a theoretical model of the unsteady aerodynamics of the airfoil over a broad range of wavenumbers. The validation and development of these models requires data and understanding from experiments. This paper is Part 1 in a two part series (Part 2 [2]) that experimentally investigates the response of an airfoil encountering turbulence under varied mean loading with the goal of providing understanding and data for development and improvement of unsteady airfoil response models. Together these two papers summarize work presented by Mish [3].

*Corresponding author. Tel.: +1 410 279 8772.
E-mail address: pmish@vt.edu (P.F. Mish).

0022-460X/$ - see front matter © 2005 Published by Elsevier Ltd.
doi:10.1016/j.jsv.2005.08.008

Nomenclature

$E[\,]$	expected value
A, B	non-dimensional coefficients of equation describing the variation in $\bar{L}^2$
b	half chord, $c/2$ (m)
c	airfoil chord (m)
C_L	mean lift coefficient per unit span, L/qc
d_s	distance along airfoil surface to pressure measurement location (m)
f	frequency, $\omega/2\pi$ (Hz)
G	airfoil response function (also referred to as blade response function and transfer function)
G_{LL}	power spectral density of lift such that $\bar{L}^2(\alpha) = \int_0^\infty G_{\mathrm{LL}}(\alpha,\omega)\,\mathrm{d}\omega$ ($\mathrm{Pa^2/m^2\,Hz^2}$)
G_{NN}	normal-to-airfoil chord force spectrum ($\mathrm{Pa^2/m^2\,Hz^2}$)
G_{pp}	surface pressure auto-spectrum such that $\bar{p}'^2 = \int_0^\infty G_{pp}(\omega)\,\mathrm{d}\omega$ ($\mathrm{Pa^2/Hz}$) (see also Appendix A)
$G_{P_UP'_U}$	surface pressure cross-spectrum on upper surface of airfoil and equivalent to S_{qq} ($\mathrm{Pa^2/Hz}$)
$G_{P_LP'_L}$	surface pressure cross-spectrum on lower surface of airfoil and equivalent to S_{qq} ($\mathrm{Pa^2/Hz}$)
$G_{P_UP'_L}$	surface pressure cross-spectrum between pressure measured on upper and lower surface ($\mathrm{Pa^2/Hz}$)
G_{TN}	cross-spectrum between normal-to-airfoil chord force and tangent-to-airfoil chord force ($\mathrm{Pa^2/m^2\,Hz^2}$)
G_{TT}	tangent-to-airfoil chord force spectrum ($\mathrm{Pa^2/m^2\,Hz^2}$)
$G_{\Delta P\Delta P}$	pressure difference auto-spectrum ($\mathrm{Pa^2/Hz}$), see also Appendix A
i	$\sqrt{-1}$ or, if subscripted, tensor notation index corresponding to 1, 2, 3
k_a	acoustic frequency, $w_a\omega_r$
K_x	wavenumber in x direction, $2\pi f/U$ (1/m)
k_x, k_y, k_z	wavenumber vector components in the x, y, z direction (1/m)
L	mean lift per unit span (N/m)
L'	unsteady lift per unit span (N/m)
$\bar{L}^2$	mean square lift, $L^2(\alpha) = \int_0^\infty G_{\mathrm{LL}}(\alpha,\omega)\,\mathrm{d}\omega$ ($\mathrm{Pa^2/m^2}$)
m_n	unique number given to each microphone
M	mach number
M_s	Sennhieser microphone calibration
N	number of ensemble averages
N_a	normal-to-airfoil chord unsteady force (N/m)
N_s	record length
P	magnitude of fluctuating surface pressure (Pa)
p'	fluctuating surface pressure (Pa)
P_L, p_L	fluctuating surface pressure on lower surface of airfoil (Pa)
P_U, p_U	fluctuating surface pressure on upper surface of airfoil (Pa)
$\bar{p}^2$	mean square pressure, $\int_0^\infty S_{qq}(x = x', \eta = 0, \omega)\,\mathrm{d}\omega$ ($\mathrm{Pa^2}$)
q	free-stream dynamic pressure, $1/2\rho U_\infty^2$ (Pa)
Re	Reynolds number based on airfoil chord, $U_\infty c/\nu$
S_{qq}	cross-spectral density of surface pressure fluctuations ($\mathrm{Pa^2/Hz}$), see also Appendix A
S^{Δ}_{qq}	cross-spectral density of pressure difference fluctuations ($\mathrm{Pa^2/Hz}$), see also Appendix A
S_R	sampling rate (Hz)
t	time (s)
T_a	tangential-to-airfoil chord unsteady force (N/m)
U_∞	mean free-stream velocity in x direction (m/s)
v_m	microphone output voltage (V)
w_a	$\sqrt{(M_\infty/\beta^2)^2 - (k_y/\beta)^2}$
ΔP	pressure difference, $P_L - P_U$ (Pa)
α	angle of attack (deg.)
β	$\sqrt{1 - M^2}$
ε_c	uncertainty in pressure spectrum based on statistical convergence
ε_r	uncertainty in pressure spectrum based on repeated measurements
ϕ_{ww}	energy spectrum of the upwash turbulence ($\mathrm{m^2/s^2}$)
η	spanwise separation between two points, $y - y'$ (m)
λ	integral scale of turbulence (m)
ν	kinematic viscosity ($\mathrm{m^2/s}$)
π	$\sim$3.14
ρ	density ($\mathrm{kg/m^3}$)
σ_a	$Mk_x/\beta k_y$
ω	angular frequency (rad/s)
ω_r	reduced frequency, $2\pi fb/U$

1.1. Review of theoretical work

The last 60 years has seen a consistent increase in the sophistication of theoretical airfoil response models. The first phase of this effort, the development of analytical methods that treats the lifting surface as a flat plate at zero angle of attack, began with the work of von Karman and Sears [4] and Sears [5], who considered the incompressible response to a two-dimensional sinusoidal upwash gust convecting with the free stream. The analyses of Possio (see the work of Graham [6]) and of Reissner [7] added compressibility effects. Graham [8] generalized the analysis to include skewed sinusoidal gusts interacting with a flat plate in incompressible flow, and then Graham [6], using similarity arguments, was able to combine this with Possio's solution to obtain the solution to the general problem of a compressible skewed gust. This phase reached its conclusion in the mid-1970s with the publication of closed-form analytic approximations to Graham's general solution. Osborne [9] and Amiet [10] developed expressions for the compressible two-dimensional gust problem, valid at low frequencies. Adamczyk [11], following on Adamczyk and Brand [12], found expressions for the skewed compressible gust response of an airfoil. Amiet [13] clarified these results and generalized them to include the case of non-convected or Kemp-type gusts [14]. Amiet and Adamczyk's results are derived using the first two steps of iterative procedures given by Landahl [15] in which the leading and trailing edge boundary conditions are alternately applied (see the work of Martinez and Widnall [16]). Their theories differ by the iterative procedure used; Amiet employs the Schwarzschild technique while Adamczyk uses the Wiener-Hopf method. Many of these theories are compared by Graham and Kullar [17]. Approximations to the incompressible skewed gust response, derived from Amiet's and Adamczyk's results and obtained by fitting Graham's results, are given by Blake [18]. Blake also describes approximate incompressible expressions due to Mugridge [19] and obtained from Liepmann [20] strip-theory generalization of the Sears result.

The second and subsequent phase of development has been driven by a desire to incorporate airfoil geometry, angle of attack effects and, in some cases, integrate aerodynamic and acoustic calculations. After some early attempts that ignored the alteration of the gust by the airfoil flow field [21,22], this phase has centered on the development of a number of sophisticated analytic and computational approaches based on Rapid Distortion Theory (RDT). Goldstein and Atassi [23], McKeough [24], and McKeough and Graham [25] were the first to use RDT to calculate the response of a lifting surface at non-zero angle of attack. Goldstein and Atassi (see also the work of Atassi [26]) considered the two-dimensional gust problem and provided separate methods for calculating the effects of angle of attack, camber and thickness. They show that the effect modeled in Horlock's theory is completely cancelled by a term arising from the distortion. McKeough and Graham [25] considered angle of attack effects on the response to a more general skewed three-dimensional gust. They concluded that in homogeneous turbulence angle of attack effects appear first in terms of order α^2. Their measurements, on a NACA 0015 airfoil in grid turbulence at one non-zero angle of attack, suggest that this is a significant effect.

The explicit application of RDT to this problem took a significant step forward with the work of Atassi and Grzedzinski [27], who proposed a novel three-way split of the fluctuating velocity field to avoid singularities at the airfoil surfaces. Subsequent efforts have invariably employed this approach, e.g. [28–34]. All of these studies are computational in nature, and have thus considered the response to disturbances at only a few discrete values of wavenumber and frequency.

1.2. Review of experimental work

Given the importance of unsteady aerodynamics it is perhaps not surprising that so many theoretical models have been developed. What is surprising, however, is the comparative lack of experimental studies suitable for validating these theories. While a number of experiments have been performed, most include only indirect observations (e.g. [35–38]), observations at only one or two disturbance wavenumbers (e.g. [39]) or at discrete frequencies in cascades [40–43] and thus do not provide a comprehensive basis for comparison.

The surface pressure measurements of Paterson and Amiet [44,45] on one side of a NACA 0012 airfoil and the NACA 0015 lift spectrum measured by Jackson et al. [46] appear to stand alone as the only direct experimental validation of flat-plate response theories over any significant wavenumber range (i.e. in turbulence). The single NACA 0015 lift spectrum measured by McKeough and Graham [25] appears to

constitute the only similar data at non-zero angle of attack. Apart from angle of attack effects, there appear to have been no in-depth studies of issues related to the non-zero thickness of any real airfoil—the finite radius of the all-important leading edge, the movement of the mean stagnation point around that radius at angle of attack, the effects of turbulence distortion here, the influence of partial or complete stall, the influence of these parameters on the relative phasing of upper and lower surface pressure fluctuations, and the influence on their spanwise correlation.

The objective of this study is to provide this missing data—to provide measurements and analysis that reveal in detail the surface pressure response of an airfoil, focusing particularly on key regions, issues, and conditions where flat-plate assumptions are invalid and where RDT or other sophisticated prediction methods must perform. To this end, measurements have been performed using an array of microphones embedded in the surface of a NACA 0015 airfoil placed at varying angles of attack in homogeneous turbulent flow. This work is presented in two parts: Part 1 presents analysis of unsteady pressure measurements with the goal of determining the effects of mean loading. Part 2 [2] of this effort discusses the likely sources of observed mean-loading effects and presents a possible model for prediction of these effects.

2. Experimental setup and techniques

2.1. Wind tunnel facility

Measurements were performed using the Virginia Tech Stability Wind Tunnel, which has a 7.32 m long square test section 1.83 m on edge. Two test section configurations were used; a solid wall configuration wherein the test section walls are formed with steel sheets (default configuration for this tunnel) and an acoustically treated configuration which utilized acoustic absorbers with screen to form the test section walls.

The default tunnel test section walls are made of steel plate on three sides with the forth side made from Plexiglas. The acoustics in the solid wall configuration at 30 m/s are quite good as shown by Larssen and Devenport [47] with peak pressure sound levels below 80 dB. Despite the relatively acoustically quiet environment offered by the solid wall configuration, wall treatment was developed to further reduce ambient noise levels. This treatment consists of a series of acoustic absorbers replacing the solid walls of the wind tunnel test section. The wind tunnel test section with absorbers attached is shown schematically in Fig. 1. The absorbers (or boxes) are made from 5/16″ fiberboard, a material often referred to as medium density fiberboard. Each box is lightly stuffed with Owens Corning 701 insulation (1.5 lb/ft^3) with a 3/4″ sheet of acoustical foam placed on top of the insulation. The acoustical foam serves as a barrier between the insulation and flow, thus minimizing the amount of airborne insulation particles. A lightweight rope is strung from side

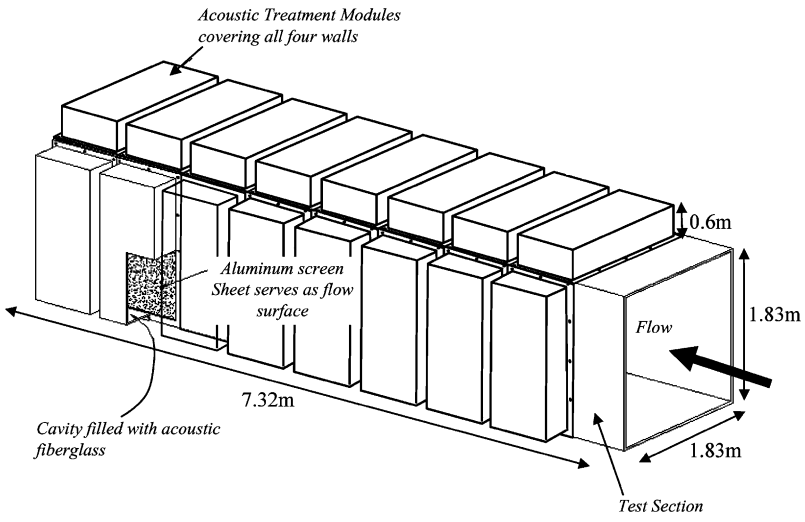

Fig. 1. Virginia Tech stability wind tunnel with acoustic absorbers attached to the test section.

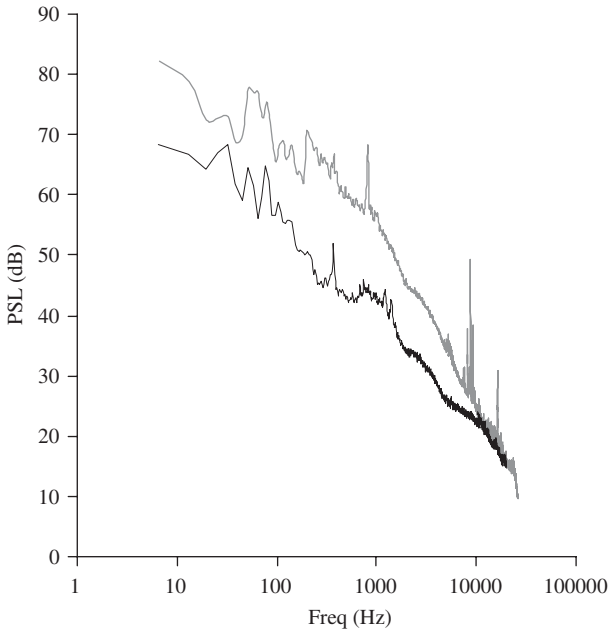

Fig. 2. Pressure sound level at 30 m/s with (—) and without (▬▬) acoustic treatment.

to side over the acoustical foam to keep the insulation and foam in place. The boxes were attached to the tunnel test section with 51 mm aluminum angle. After the boxes were mounted to the test section, sheets of aluminum screen were attached which serve as the test section wall and flow surface. The aluminum screen is 1/8″ thick with a 40% open area ratio.

The effects of the acoustic treatment modules were documented through acoustic measurements with a Bruel and Kjaer microphone. The acoustic measurements of Larssen and Devenport [47] made with the test section in solid wall configuration are compared with similar measurements in the acoustic treatment configuration. The pressure sound levels of both measurements are presented in Fig. 2 for a flow speed of 30 m/s. When the acoustic treatment is present considerable attenuation of the ambient sound field occurs between 10 and 10 kHz with as much as 20 dB of attenuation occurring between 100 and 500 Hz. The spectra appear to converge at 20 kHz.

2.2. Airfoil model

The unsteady surface pressure was measured on a 0.610 m chord, 1.83 m span, NACA 0015 airfoil model, constructed as an extruded aluminum section. The section was measured and its thickness profile was found to agree with the theoretical NACA 0015 to within 0.1% chord—the largest disagreements showing the model to be slightly thicker than the specification over the latter 30% of the chord. The model trailing edge was rounded with a radius of 2.7 mm. The model was mounted in the center of the test section with its leading edge 3.23 m downstream of the section entrance. The model completely spanned the test section and was mounted so as to allow rotation to angle of attack about its quarter chord line.

2.3. Grid-generated turbulence

For turbulence generation, a square bi-planar grid with a 305 mm mesh size and an open area ratio of 69.4% was mounted in the wind tunnel contraction 5.82 m (19.1 mesh sizes) upstream of the airfoil leading-edge location. At this point the cross-sectional area was 32% larger than that of the test section, the remaining contraction being used to improve the isotropy of the turbulence. Acoustic foam wedges attached to the downstream side of the grid were used to minimize grid-generated noise.

Table 1
Turbulence parameters

Intensity u'/U_∞	3.93%
Longitudinal scale λ (chords)	0.134
Eddy turnover distance $\lambda U_\infty/u'$ (chords)	3.4
Taylor Reynolds number	337

Detailed three-component hot-wire measurements of turbulence quantities, spectra, and space–time correlations were made with the airfoil removed, but at the leading-edge location. At 30 m/s these measurements (detailed by Bereketab et al. [48]) showed the turbulent flow to be closely homogeneous and isotropic and to have a spectral form accurately described by the von Karman interpolation formula, at least for wavenumbers within and below the inertial subrange. Turbulence parameters are listed in Table 1.

2.4. Mean pressure instrumentation

Mean loading on the airfoil was monitored during solid wall measurements with a 48-port Scanivalve system and Honeywell Model DRAL520GN pressure transducer interfaced with an IBM/AT computer through a data translation DT2801-A A/D converter. During measurements with acoustically treated walls, a Dwyer series 427 Mark III handheld digital manometer (range 0–10″ of H_2O, accuracy ± 0.01″ of H_2O) was also used to make mean pressure measurements at 23% chord. One millimeter diameter pressure taps were located in chordwise rows on both sides of the airfoil offset 355 mm from its center span. Pressure measurements were compared with panel method calculations to verify angle of attack. At higher angles of attack these measurements, in conjunction with tuft flow visualizations, were used to estimate approximate stall locations. Solid and wake blockage and streamline curvature effects are investigated by Mish [54] and found to have a negligible impact on the mean velocity field and lift.

2.5. Unsteady pressure instrumentation

Unsteady surface pressures were measured using an array of Sennheiser KE 4-211-2 microphones, embedded in the airfoil surface. Microphones were mounted 0.5 mm beneath the airfoil surface, and a 1 mm diameter pressure tap (matching the microphone pinhole size) was used to connect them to the surface. The Sennheiser KE 4-211-2 microphone is small (5 mm diameter), sensitive (10 mV/Pa), provides low noise signals and has a nominal response that is flat to within 1 dB from 40 to 10,000 Hz and calibratable over a larger range. Recessing them 0.5 mm below the surface appeared to have no significant effect on this response. Microphone signals were individually amplified using circuitry installed in the hollow interior of the blade, and the amplified signals recorded using a Hewlett-Packard E1432A based data acquisition system. This system provides simultaneous measurement of up to 64 channels with 16 bit accuracy at sampling rates up to 56 kHz per channel, and has built in anti-alias filtering.

The phase and amplitude response of every microphone was measured and monitored using a calibrator. The calibrator, based on a NASA design, contains a shallow cavity in which the microphone is centered in a narrow opening opposite small wide-range loudspeaker. The speaker is driven from an audio amplifier using a white noise signal, compensated for the response of the speaker/amplifier system, generated by the HPE1432A. By comparing the cross-spectrum between the white noise and microphone output with that obtained using a reference microphone, repeatable phase and amplitude calibrations could be obtained between 5 and 10,000 Hz. The reference was a B&K model 4138 1/8″ diameter microphone.

2.6. Microphone distribution

Measurements of unsteady surface pressure were made in the solid wall configuration using an array of 96 microphones (48 per side with each side a mirror image of the other) distributed, as shown in Fig. 3. The origin in Fig. 3 is taken as the leading edge and mid-span with x directed downstream and y directed along the airfoil

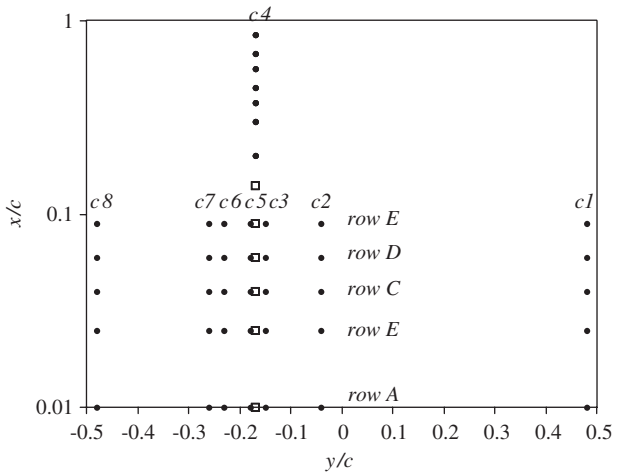

Fig. 3. Distribution of microphone in airfoil during solid wall test. Total of 96 microphones used with 48 per side and each side is a mirror image of the other. □, microphones used in unsteady lift calculation.

span. Microphones are located in chordwise rows between 1% and 85% chord from the leading edge, at spanwise separations of between 1% and 96% chord. The spanwise distribution of microphones is designed to take advantage of the homogeneity of the flow in this direction so that the eight spanwise stations together define some 25 approximately logarithmically spaced spanwise separations.

A complimentary set of unsteady pressure measurements was made with the solid walls replaced by acoustic treatment modules. These measurements were performed with an array of 40 microphones that used *row B* and column *c4* of Fig. 3.

2.7. Test matrix

2.7.1. Solid wall test

Measurements were made with the wind tunnel in solid wall configuration at angles of attack, $\alpha = 0^\circ$, 4°, 8°, 12°, 16°, and 20°. The nominal flow velocity was 30 m/s corresponding to a chord Reynolds number of 1.17×10^6. Two sampling rates were used to gather data: 1.6 and 12.8 kHz. Five hundred records of data were taken with a record length of 2048 samples.

Simultaneous measurement of all 96 microphones was not possible due to the data acquisition systems 64 channel capacity. Therefore, measurements were made in three microphone blocks with the longest chordwise column (*c4* of Fig. 3) of microphones common to each. Block one measured the first two spanwise rows (*row A* and *B*), block two the third and forth spanwise rows (*row C* and *D*), and block three the fifth spanwise row (*row E*). Some measurements also used a forth block of microphones which was composed of rows *B* and *D*.

Several subsets of unsteady pressure data were taken under alternate configurations. To aid in assessing noise in unsteady pressure measurements, data were taken with the turbulence generating grid removed. Two types of measurements were made in this configuration. One matched the flow velocity of 30 m/s which aids in assessing contamination associated with boundary layer pressure fluctuations. The other matched the tunnel fan speed (rpm) achieved when the grid is installed which aids in determining the extent of ambient acoustic field contamination. Table 2 summarizes the angle of attacks, microphone configuration, sampling rates, and grids used in each solid wall measurement.

2.7.2. Acoustically treated wall test

A second set of measurements was made with the steel test section walls replaced by acoustic treatment at angles of attack, α from 0° to 20° in 2° increments. Two sampling rates were used for these measurements: 1.6 and 25.6 kHz. One-thousand records were taken with a record length of 2048.

Table 2
Solid wall test configuration details

Measurement	Angle of attack (deg.)	No. of Mics	Microphones used. Definitions refer to Fig. 4	Sampling rate (kHz)
Unsteady pressure	0, 4, 8, 12, 16, 20	96	*c4* and *rows A–E*	1.6
			c4 and *rows A* and *B*	12.8
Smooth flow	0, 4, 8, 12, 16, 20	54	*c4* and *rows B* and *D*	1.6
Matched RPM	0	54	*c4* and *rows B* and *D*	1.6

Table 3
Uncertainties in unsteady pressure spectra

ω_r	ε_r at $x/c = 0.1$ ($\pm$dB)	ε_r at $x/c = 0.4$ ($\pm$dB)
1	0.58	0.92
10	0.49	0.40
35	0.81	0.18

Additionally, measurements were performed at $\alpha = -4^\circ$ and -8°, although these data are not presented here (see the work of Mish [3]). A boundary layer trip was incorporated into a set of measurements covering $\alpha = -8^\circ$, -4°, and 4°. For this set of measurements, a sampling rate of 1.6 kHz with a record length of 2048 was used to take 200 records of data.

Oil flow visualization was performed over a range of angles of attack including $\alpha = 0^\circ$, $\pm 4^\circ$, $\pm 8^\circ$, $\pm 12^\circ$, 16°, 20° and is presented by Mish [3].

2.8. Measurement uncertainty

An estimate of the uncertainty in unsteady pressure measurements was made through analysis of multiple measurements, calibration and normalizing quantities uncertainty, and variations in ambient conditions. Uncertainty in the *pressure difference* spectra (see Appendix A for precise spectral definition of pressure difference), ε_r at 20 to 1 odds are presented in Table 3.

Some spectra were spanwise averaged to reduce uncertainty. The reduction in uncertainty based on statistical convergence is given by Bendat and Piersol [49] as

$$\varepsilon_c = \frac{\varepsilon_r}{\sqrt{N}}, \tag{1}$$

where $N = 8$ (the number of microphones in a spanwise row). In these cases, spanwise averaging reduces spectral uncertainty to a fraction of a decibel.

2.9. Data contamination and quality

This experiment sets out to measure the inviscid response of an airfoil in turbulence using microphones. The expectation here is that the microphones will measure pressure fluctuations associated with the non-penetration condition. However, measurements of unsteady pressure made with microphones are subject to a variety of contamination sources such as wind tunnel acoustic field, boundary layer, stall, convection of eddies, and electrical noise.

The results of Mish's [3] investigation of contamination and data quality are summarized here. Unsteady pressure data are shown to be free of acoustic contamination based on comparisons with measurements of unsteady pressure made without the turbulence generating grid, at the same free-stream conditions and at the same wind-tunnel fan rpm. Additionally, spectra measured at the leading-edge stations (1% and 2.5% chord) were found to be free of airfoil boundary layer and free-stream eddy convection pressure fluctuations. Pressure measurements from 4% to 14% chord were found to be free of such contamination for $\omega_r < 10$. These

conclusions were supported by space–time correlation maps of surface pressure fluctuations which showed the inviscid response to be dominant in unsteady pressure measurements at all unstalled angles of attack.

3. Unsteady loading prediction schemes

Two theoretical solutions to the problem of an airfoil encountering turbulence are presented and used for comparison with unsteady pressure measurements. The linearized, inviscid theory developed by Amiet [50,51] for a flat plate with zero-mean loading is discussed. This theory is currently used by many aeroacoustics engineers and therefore will be directly compared with experimental results. A more sophisticated theory that incorporates the effects airfoil mean loading is also presented. The formulation is from Reba and Kerschen [52] and uses RDT to predict the response of a flat plate in turbulence. Direct comparison of this theory with measured data is not appropriate due to a limitation in a numerical function; however, predicted angles of attack trends are used for discussion with measured data.

3.1. Zero-mean-loading predictions

For the relatively easier scenario of a flat plate at *zero angle of attack*, Amiet [50,51] derived one of the most commonly used solutions to the problem. Amiet reworks Filotas' [53] result into two solution regions; one which is valid at small spanwise wavenumbers (k_y) and the other at large spanwise wavenumbers giving essentially a complete low to high frequency solution to the problem of a flat-plate airfoil encountering a skewed gust. This complete solution, valid for both small and large spanwise wavenumbers, is derived by Mish [54] in terms of the airfoil response function g and is repeated here for completeness:

$$g(x,k_x,k_y)=-\frac{f(x,k_x,k_y)}{\pi\,\beta}\left\{\pi x\left[\left(k_y^2\big/\beta^2-\mu^2\right)^{1/2}+\mathrm{i}(\mu M+k_x)\right]\right\}^{-1/2}\mathrm{e}^{-x\left(k_y^2/\beta^2-\mu^2\right)^{1/2}+\mathrm{i}\mu Mx}, \tag{2}$$

where

$$f(x,k_x,k_y)=1-(x/2)^{1/2}\left\{1-\mathrm{erf}\left[\left(2(2-x)\left(k_y^2\big/\beta^2-\mu^2\right)^{1/2}\right)^{1/2}\right]\right\}$$

when $k_y\geqslant(M/\sqrt{1-M^2})k_x$, and

$$f(x,k_x,k_y)=1-(x/2)^{1/2}\left\{1-(1-\mathrm{i})E\left[2\mathrm{i}\left(\frac{1}{\pi}(2-x)\left(\mu^2-k_y^2\big/\beta^2\right)^{1/2}\right)^{1/2}\right]\right\}$$

otherwise. In these equations, $\mu=Mk_x/\beta^2$ and $E[\,]$ is the Fresnel integral function. The pressure difference is then given, based on the work of Amiet [51] with coordinate system origin at mid-chord, as

$$\Delta P(x,y,t,k_x,k_y)=2\pi\rho_0 U w_0 g(x,k_x,k_y)\,\mathrm{e}^{\mathrm{i}(k_x Ut-k_y y)}. \tag{3}$$

The final form of the pressure jump cross-spectrum, S_{qq}^{Δ}, is obtained for a single-sided spectrum (i.e. positive frequencies only) as a function of frequency f in Hertz as

$$S_{qq}^{\Delta}(x,x',\eta,f)=16\pi U(\pi\rho b)^2\int_0^{\infty}g^*(x',K_x,k_y)g(x,K_x,k_y)\Phi_{ww}(K_x,k_y)\mathrm{e}^{\mathrm{i}k_y\eta}\,\mathrm{d}k_y, \tag{4}$$

where $\eta=y-y'$, $K_x=2\pi f/U$, and Φ_{ww} is the energy spectrum of the turbulence.

To compare with the measurements made using the microphone array, a MATLAB code to predict the unsteady surface pressure field using the combined theoretical approach of Amiet [50,51] was developed and uses the above formulation of S_{qq}. Amiet's [50,51] prediction scheme requires inputs related to form of the turbulence spectrum, its length scale and turbulence intensity, and half chord of the modeled airfoil. All input parameters are summarized in Table 4.

Table 4
Summary of input parameter used in Refs. [50,51] prediction code

Input parameter	Value
Turbulence spectral form (Φ_{ww})	von Karman as given by Paterson and Amiet [44]
Free-stream velocity, U_∞	30 m/s
Length scale, λ	81.8 mm
Intensity, u'/U_∞	3.93%
Semi-chord, b	305 mm
η	0
x/c	1%, 2.5%, 4%, 6%, 9%, 14%
k_x	0.21–2100, logarithmically spaced
k_y	0.0003–3280, in steps of 0.16

3.2. Non-zero-mean-loading predictions

The theory considered here was developed by Kerschen and Myers [56], Myers and Kerschen [30], and Reba and Kerschen [52] for application to a flat-plate airfoil subject to some mean loading. A solution is derived for the unsteady pressure distribution on the airfoil surface due to interaction with a three-dimensional time harmonic gust. The airfoil is assumed to be a zero thickness flat plate at some mean angle of attack to a subsonic inflow. The distortion of the inflow by the mean field velocity gradients is accounted for using RDT. Singular perturbation expansions are developed for the case of Mach number of order 1, wherein the acoustic wavelength is short compared to the airfoil chord and for the case of small Mach number, in which the acoustic wavelength is long compared to the airfoil chord. As such, the airfoil–gust interaction analysis is simplified in various asymptotic limits at high and low acoustic frequencies. For the case of $M_\infty \ll 1$ (the case for the present experiment, $M_\infty = 0.087$), the low acoustic frequency limit is applied. In doing so the gust may be two or three dimensional; however, due to the relationship between the acoustic frequency and spanwise wavenumber a three-dimensional gust is limited to only very small spanwise wavenumbers.

Reba and Kerschen [52] developed a FORTRAN computer routine for their theory which is utilized in a modified form to compute the predicted cross-spectrum of surface pressure fluctuations, S_{qq}. The final form of S_{qq} is given here in terms of modified pressure as

$$S^{\Delta}_{qq}(x, x', \eta, \omega_r) = (U_\infty \rho)^2 \int_{-\infty}^{\infty} \int_{-\infty}^{\infty} (p_{\mathrm{Uua}} - p_{\mathrm{Lua}})(p'_{\mathrm{Uua}} - p'_{\mathrm{Lua}})^* \phi_{ww}(\omega_r, k_3)\, \mathrm{e}^{\mathrm{i}\hat{k}_3 \eta}\, \mathrm{d}k_n\, \mathrm{d}k_3, \tag{5}$$

where p_{Uua} and p_{Lua} are the modified pressures computed for a unit amplitude inflow on the upper and lower surfaces, respectively. To avoid confusion it is worth noting, explicitly, that Eq. (5) is for a double-sided spectrum in frequency ($-\infty < \omega_r < \infty$) and therefore is multiplied by 2 when calculated to obtain a single-sided spectrum for comparison purposes. Comparisons with measured data are made using the modified Reba and Kerschen FORTRAN code with parameters listed in Table 5.

4. Basic aerodynamic features

4.1. Mean lift

Mean pressure measurements on the NACA 0015 are summarized here (discussed in detail by Mish [54]) through the presentation of mean C_L versus angle of attack. Fig. 4 presents lift coefficients for $\alpha = 0^\circ$, 4°, 8°, 12°, 16°, and 20° calculated from integrating mean pressure measurements. Also shown in Fig. 4 are the mean C_L values for various measurements made by McKeough [24] with a NACA 0015 in various scale and intensity turbulent flows. The theoretical lift curve [55], $2\pi\alpha$, is also plotted in Fig. 4. The flow appears to remain largely attached and the airfoil is unstalled up to $\alpha = 12^\circ$. Beyond $\alpha = 12^\circ$ significant separation appears to occur resulting in a reduction of C_L at $\alpha = 16^\circ$ and finally complete stall at $\alpha = 20^\circ$.

Table 5
Summary of input parameter used in Ref. [52] prediction code

Parameter	Value
Turbulence spectral form (Φ_{ww})	von Karman as given by Paterson and Amiet [44]
M_∞	0.087
Length scale, λ	81.8 mm
Intensity, u'/U_∞	3.93%
Semi-chord, b	305 mm
η	0
x/c	1%, 2.5%, 4%, 6%, 9%, 14%
α	0°, 2°, 6°
$k = I$	Where $i = 1, 2, 3, \ldots, 10$
$k_3 = \dfrac{10[(j-1)\Delta k_3]}{k}$	Where $j = 1, 2, 3, \ldots, 41$ and $\Delta k_3 = 0.01$
$k_n = \dfrac{10[(l-1)\Delta k_n]}{k}$	Where $l = 1, 2, 3, \ldots, 30$ and $\Delta k_n = 0.06$

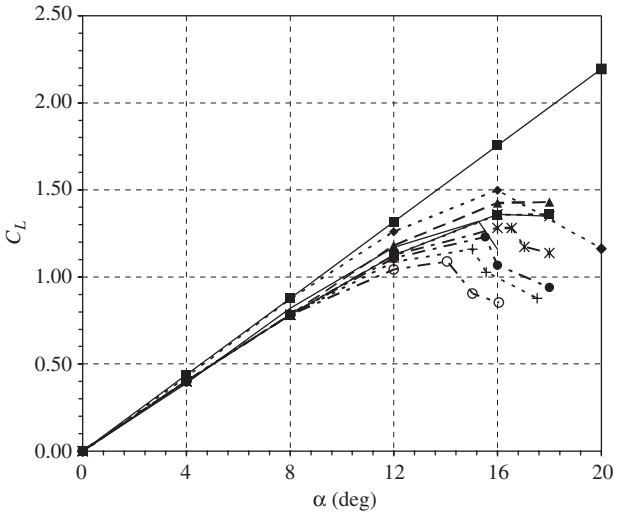

Fig. 4. Mean lift coefficient calculated from mean pressure measurements (- - ◆ - ·) compared with those measured by McKeough's [24] (- - ■ - ·, GL; — ▲ —, GS1; ——✕——, GS2; — ✱ —, GS3; — ●— -, GS4; - - + - ·, GS6; — ○—, smooth LR; —, smooth HR) and thin airfoil theory (——■——). The notation GL and GS is used by McKeough to describe differences in turbulence intensity and length scale. LR (low Reynolds number) = 0.26 mil and HR (high Reynolds number) = 0.76 mil.

4.2. Stagnation, transition, and separation points

The stagnation, transition, and separation locations are presented here (discussed in detail by Mish [54]) in Fig. 5. This figure shows a cross-section of the airfoil with the locations of transition, stagnation, and separation denoted by symbols along the edge of the airfoil. The transition locations, determined from high pass filtered pressure time series, are shown to shift down the chord on the pressure side as the angle of attack is increased while moving toward the leading edge on the suction side. Oil flow visualizations and fluctuating pressure measurements hinted at the presence of unsteady laminar separation bubble on the suction side of the airfoil leading edge between 1% and 3% chord for at all non-zero angles of attack up to 12° (not shown in Fig. 5 due to its uncertain location). At $\alpha = 16°$ a much larger leading-edge separation bubble was formed, reattaching at 9% chord and producing a loss of pressure over the first 5% chord. The flow separates again in this case near the 50% chord station. At $\alpha = 20°$ the flow is stalled over the entire suction side.

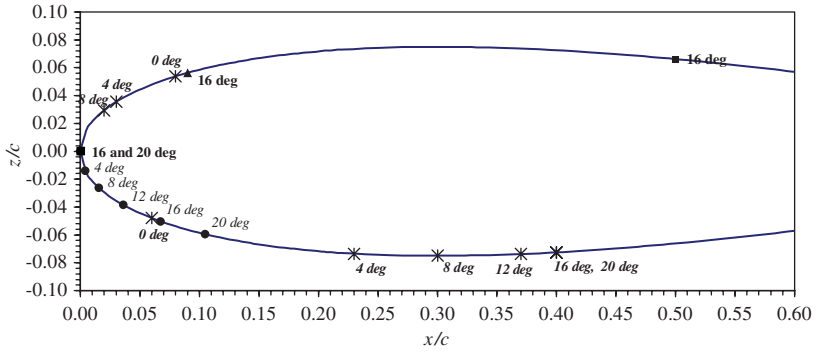

Fig. 5. Stagnation (●), transition (∗), separation locations (■), and reattachment points (▲) along the surface of the NACA 0015 airfoil (—).

5. Unsteady pressure measurement results and discussion

This section presents analysis of unsteady surface pressure measured on the NACA 0015 airfoil in grid-generated homogeneous turbulence at angles of attack, $\alpha = 0-20^\circ$. Zero angle of attack measurements are presented first, and compared with predictions from Amiet's [50,51] flat-plate, zero-mean load theory. Effects of angle of attack on pressure spectra are then examined and comparisons made with Reba and Kerschen's [52] unsteady loading theory. Angle of attack effects are summarized with lift spectra calculated from measured unsteady pressures and are compared with Amiet's [50,51] theory for $\alpha = 0^\circ$ and Reba and Kerschen's [52] theory at non-zero angle of attack.

5.1. Pressure spectra and mean square pressure

5.1.1. Pressure difference spectra at zero angle of attack

Measured pressure spectra at $\alpha = 0^\circ$ are compared with Amiet's [50,51] theory in this section. Fig. 6(a)–(f) presents a comparison of Amiet's predicted *pressure difference* spectra (see Appendix A for definition of pressure difference) with measured *pressure difference* spectra at $\alpha = 0^\circ$ for chordwise locations, $x/c = 1\%$, 2.5%, 4%, 6%, 9%, and 14% normalized on free-stream dynamic pressure, q. Both the measurement and prediction fall monotonically moving away from the leading edge. At all chordwise locations Amiet's theory agrees well with the measured shape of $G_{\Delta P \Delta P}$ spectra and reasonable agreement in level is achieved. The theory tends to over predict spectra levels at 1% chord (Fig. 6(a)) with as much as 4 dB of difference occurring here. The over prediction of surface pressure at 1% chord is likely the consequence of the leading-edge singularity which occurs in Amiet's theory. The agreement in spectral level improves to within 1 dB moving away from the leading edge. The measured data tend to roll off slightly faster than the prediction over $5 < \omega_r < 20$. The disagreement in slope may be a result of the airfoil thickness. Other researchers have shown similar results, although unpublished [57,58]. The slope of the measured data decreases for $\omega_r > 20$. The change is subtle for the first four chordwise locations (Fig. 6(a)–(d)) and may be related to the pressure signatures of eddies convecting past the airfoil nose. At $x/c = 9\%$ and 14% (Fig. 6(e)–(f)) the slope changes substantially more for $\omega_r > 20$ as significant boundary layer pressure fluctuations begin to affect the high frequency response.

At some chordwise locations a high frequency spike is present in measured $G_{\Delta P \Delta P}$. This spike, occurring over a range of $300 < \omega_r < 800$ appears to be related to resonance within the microphone mounting hole that was not accounted for in the microphone calibration.

5.1.2. Mean square pressure at zero angle of attack

The dependence of $\alpha = 0^\circ$ root-mean square (rms) pressure fluctuations on chordwise location is presented in Fig. 7. Pressure difference spectra at each chordwise location are integrated to obtain mean

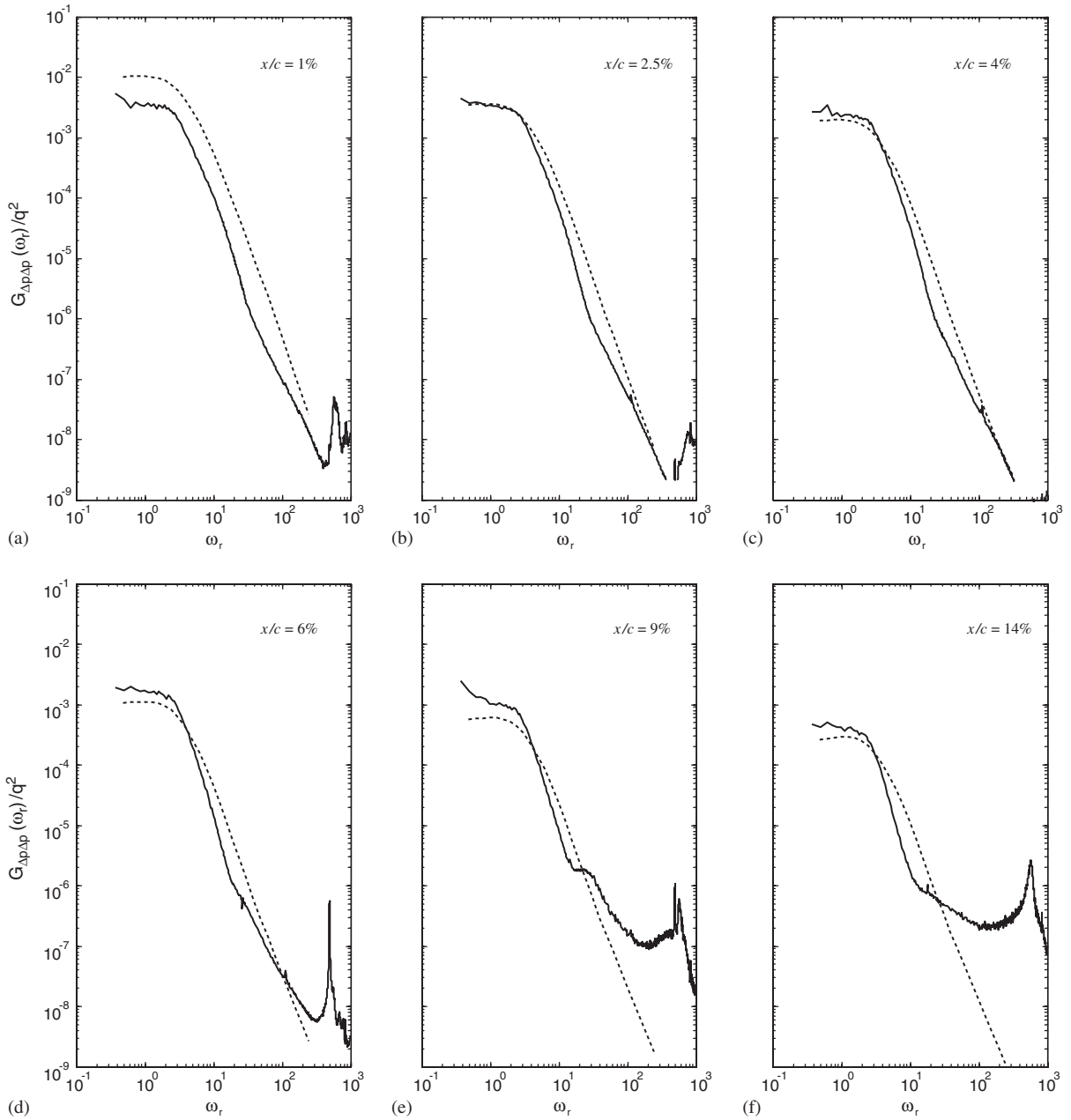

Fig. 6. Plots of measured pressure difference spectral level (—, measurement) compared with Amiet's theory (▪▪▪▪▪▪, Amiet) for $\alpha = 0^\circ$ at $x/c =$ (a) 1%, (b) 2.5%, (c) 4%, (d) 6%, (e) 9%, and (f) 14% chord.

square p' values as

$$\bar{p}^2(x) = \int_{f_{\min}}^{f_{\max}} S^{\Delta}_{qq}(x, x', \eta, f)\, \mathrm{d}f, \tag{6}$$

where S^{Δ}_{qq} is the *pressure difference* cross-spectral density, $x = x'$, and $\eta = 0$. The integration is performed from a minimum frequency, $f_{\min} = 6\,\mathrm{Hz}$ ($\omega_r = 0.4$) to a maximum frequency, $f_{\max} = 1570\,\mathrm{Hz}$ ($\omega_r = 100$). Measured

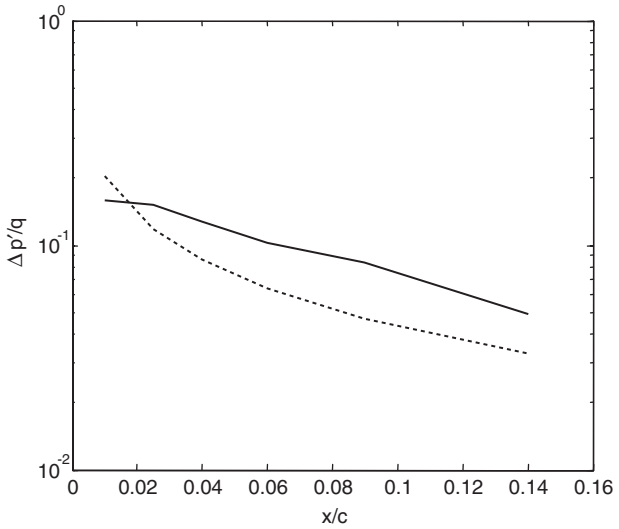

Fig. 7. Measured root-mean square of p (—, measurement) as a function of x/c at $\alpha = 0^\circ$, formed from integrating pressure spectrum over $\omega_r = 0.4-100$. Comparison is made with Amiet's theory (▪▪▪▪▪▪, Amiet).

values are also compared with those calculated from Amiet's [50,51] theory and are normalized on free-stream dynamic pressure, q. Measured rms pressure shows a near linear (on this log plot) dependence on chordwise location with peak rms values occurring in the leading-edge region. The agreement of p' values with Amiet's prediction is within 3 dB across the much of the chord. In the leading-edge region Amiet's prediction begins to rise rapidly as a consequence of the leading-edge singularity in this theory.

5.1.3. Pressure difference spectra at non-zero angle of attack

Measured pressure spectra are compared with Reba and Kerschen's [52] linearized RDT predictions for similar chordwise locations and angles of attack. A modified version of the FORTRAN code produced by Reba and Kerschen [52] is used to calculate the airfoil response from which the pressure difference cross-spectral density is computed. However, due to the restriction in Reba and Kerschen's theory of low acoustic wavenumber it is not possible to integrate over a large range of spanwise wavenumbers. Consequently, the absolute levels of predictions from Reba and Kerschen's theory are somewhat questionable. As such, a direct comparison between predicted and measured unsteady pressure level is not appropriate, although a comparison of spectral shape and variation with angle of attack and chordwise position seems reasonable.

Fig. 8(a)–(f) presents measured *pressure difference* spectra as a function of frequency at six chordwise ($x/c = 1\%$, 2.5%, 4%, 6%, 9%, 14%) locations and all measured angles of attack ($\alpha = 0-20^\circ$) plotted with predicted spectra for $\alpha = 0^\circ$, 2°, and 6°. All spectra are normalized on free-stream dynamic pressure, q, and the prediction frequency axis is multiplied by a factor of 10 for clarity. The most striking observation shown in Fig. 8(a)–(f) is the reduction in spectral level at low reduced frequencies ($\omega_r < 5$) that occurs as the angle of attack increases at all chordwise stations. This reduction is on the order of 5 dB and has never before been shown either experimentally or theoretically. Equally interesting is that as α increases, spectral levels fall by an increasing amount which suggests perhaps an α^2 dependence as proposed by McKeough and Graham [25]. For higher reduced frequencies ($\omega_r > 5$) a significant rise in spectral level occurs at all chordwise location as the angle of attack is increased. The slope of spectra also begins to decrease in this frequency range. The change in slope at high frequencies may be related to boundary layer and eddy convection pressure fluctuations.

Reba and Kerschen's predicted spectra fall monotonically moving away from the leading edge at all angles of attack, as shown to occur in measured data. Additionally, the spectra show a somewhat flat range for $\omega_r < 2$ and then begin to fall off with a slope similar to that shown in measured data. Perhaps most notable, though, is the stark contrast in measured and predicated effects of angle of attack on pressure spectra. Reba and Kerschen's theory predicts a large rise in spectral level with increasing angle of attack that is particularly dominant at low reduced frequencies, with up to a 16 dB increase, and occurs at all chordwise locations. The

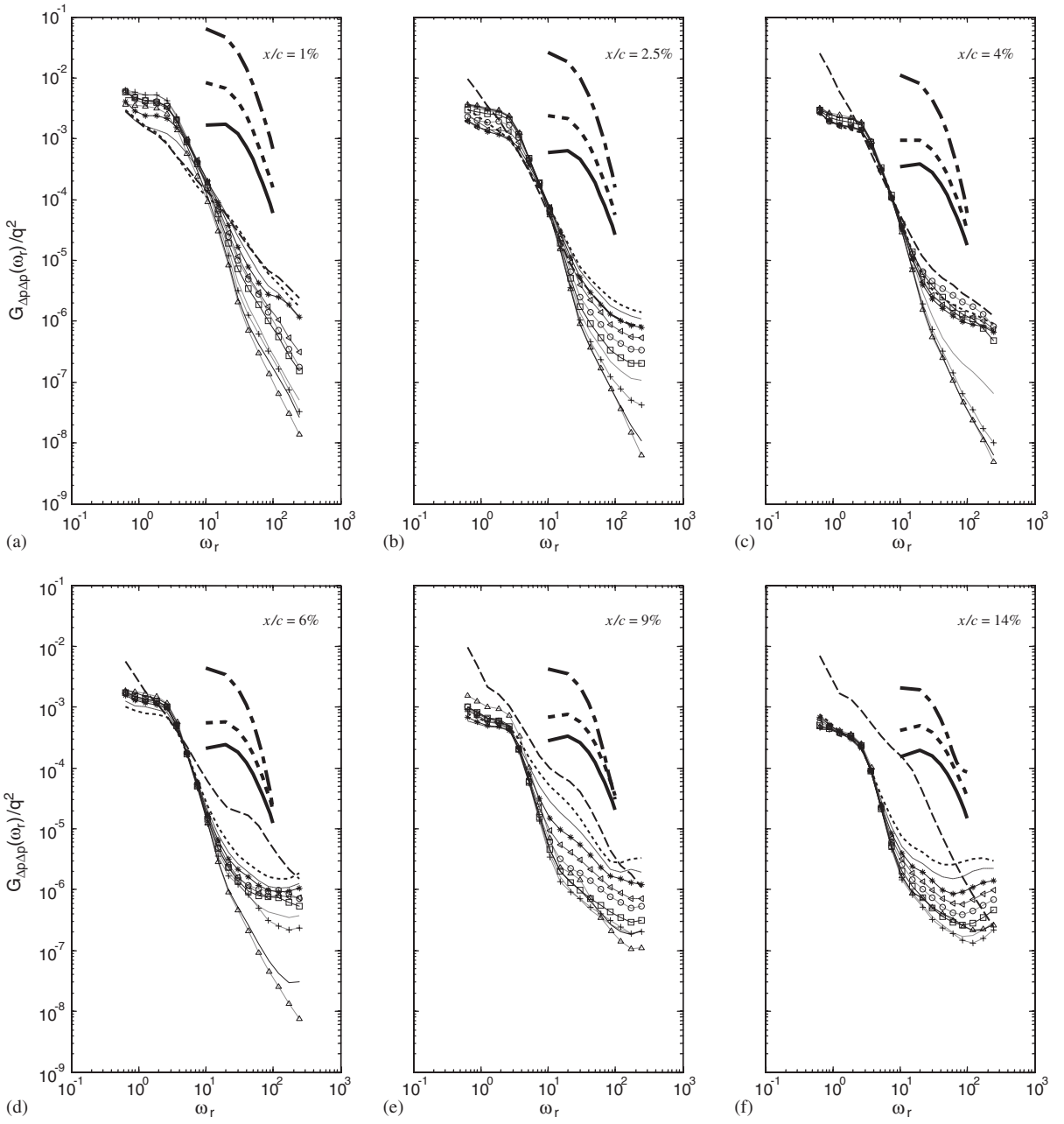

Fig. 8. Plots of measured pressure difference spectral level (--△--, $\alpha = 0°$; —, $\alpha = 2°$; --+--, $\alpha = 4°$; ……, $\alpha = 6°$; –□–, $\alpha = 8°$; --○--, $\alpha = 10°$; —◁—, $\alpha = 12°$; —✳—, $\alpha = 14°$; — — —, $\alpha = 16°$; ▪▪▪▪, $\alpha = 18°$; ▬▪▬, $\alpha = 20°$) compared with Reba and Kerschen's theory (▬, $\alpha = 0°$; ■ ■ ■, $\alpha = 2°$; ▬ ■, $\alpha = 6°$) at $x/c =$ (a) 1%, (b) 2.5%, (c) 4%, (d) 6%, (e) 9%, and (f) 14% chord. Frequency axis of predictions is shifted by a factor of 10 to the right.

spectral levels tend to converge at higher reduced frequencies and seem to better capture the measured angle of attack effects here. The reason for the large change in spectral level predicted by Reba and Kerschen [52] with increasing angle of attack may be related to the flat-plate model they assume. The potential field associated with a flat plate with leading-edge singularity will distort the inflow substantially more than an actual airfoil with thickness due to the very large velocity gradients that stretch and tilt the vorticity vectors of the inflow

turbulence in the vicinity of the leading-edge singularity. This result seems to indicate a flat-plate model is not adequate for predicting mean-loading effects for the present experiments inflow scale to airfoil chord ratio.

Furthermore, since pressure spectral levels fall only slightly for small angles of attack ($\alpha < 8^\circ$) at low reduced frequencies, the zero-mean-loading theory of Amiet [50,51] may be sufficient for predicting the airfoil response when the angle of attack is small and the relative scale of the inflow to airfoil chord is near that in the present experiment. A similar conclusion is put forth by Paterson and Amiet [44].

5.1.4. Mean square pressure at non-zero angle of attack

The effects of angle of attack on p' values are investigated in Fig. 9. rms pressures, $\sqrt{\Delta p'^2}$, calculated from *pressure difference* spectra are presented in Fig. 9. It is interesting to see that rms $\Delta p'^2$ remain essentially flat up to $\alpha = 14^\circ$ at all chordwise locations. A slight rise occurs at $x/c = 1\%$ between 0° and 4° angle of attack. The $\sqrt{\Delta p'^2}$ lack of dependence on angle of attack suggests the increased eddy stretching (by the mean velocity field) that likely takes place with increasing angle of attack does not substantially increase the intensity of pressure fluctuations in the leading-edge region.

5.2. Lift spectra and verification of lift formulation

The effects of angle of attack on the surface pressure response can be well summarized by investigating the unsteady lift calculated from unsteady pressure measurements. Such a calculation inherently contains surface pressure and pressure difference auto- and cross-spectra and provides an integrated view of the airfoil response.

5.2.1. Unsteady lift formulation and verification

This section presents the equations for calculating lift from unsteady pressure measurements and addresses issues associated with such calculations. Integration of stochastic quantities is not a trivial matter and as such, considerable effort is spent in identifying sources of error and verifying results.

Unsteady lift is calculated from pressure measurements made over the first 14% of the airfoil chord. This corresponds to six microphones per airfoil side used in the calculation. The microphones used in the lift calculation are denoted in Fig. 3 by squares and their chordwise and spanwise locations are presented in Table 6. The unsteady pressure measurements must first be resolved into normal-to-chord and

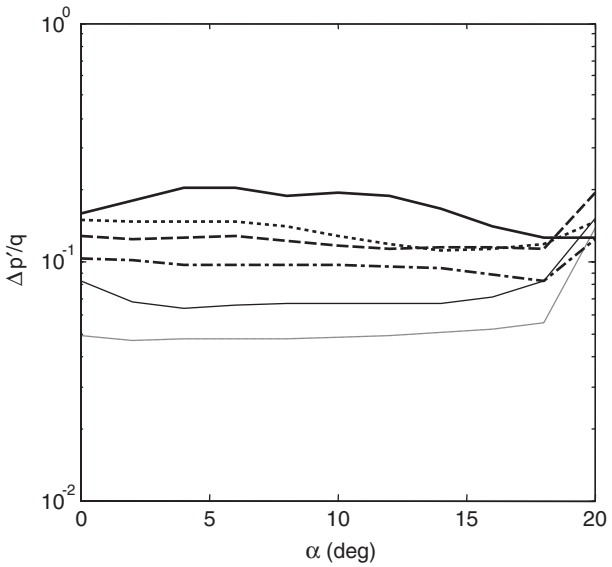

Fig. 9. Root-mean square of p as a function of α for each chordwise location (——, $x/c = 1\%$; ·····, $x/c = 2.5\%$; – – –, $x/c = 4\%$; –·–·–, $x/c = 6\%$; —, $x/c = 9\%$; ……, $x/c = 14\%$). rms values obtained from integrating pressure spectra over $\omega_r = 0.4-100$.

Table 6
Location of microphones used in unsteady lift calculation

y/c	x/c
−0.17	0.01
−0.17	0.025
−0.17	0.04
−0.17	0.06
−0.17	0.09
−0.17	0.14

tangential-to-chord force components. The relationship between these forces and lift is a simple coordinate transformation from airfoil to flow-aligned coordinates given as

$$L' = N_a \cos(\alpha) - T_a \sin(\alpha), \tag{7}$$

where L' is the lift and α is the angle of attack. Since the lift is a random quantity the expected value is taken to give the lift spectrum,

$$\begin{aligned} G_{\mathrm{LL}} &= E\left[L'^{*}L'\right] \\ &= E[N_a^{*}N_a\cos^2(\alpha) + T_a^{*}T_a\sin^2(\alpha) - T_a^{*}N_a\sin(\alpha)\cos(\alpha) - N_a^{*}T_a\sin(\alpha)\cos(\alpha)] \\ &= G_{\mathrm{NN}}\cos^2(\alpha) + G_{\mathrm{TT}}\sin^2(\alpha) - 2Re(G_{\mathrm{TN}})\sin(\alpha)\cos(\alpha). \end{aligned} \tag{8}$$

G_{NN} and G_{TT} are the normal and tangential force spectra and G_{TN} is the cross-spectrum between these forces. These spectra can be computed from unsteady pressure measurements as

$$\begin{aligned} G_{\mathrm{NN}}(\omega_r) &= E\left[\int_0^{x_{\max}}\int_0^{x_{\max}} \Delta P(x,\omega_r)^{*}\Delta P(x',\omega_r)\,\mathrm{d}x\,\mathrm{d}x'\right] \\ &= \int_0^{x_{\max}}\int_0^{x_{\max}} G_{\Delta P\Delta P'}(\omega_r,x,x')\,\mathrm{d}x\,\mathrm{d}x', \end{aligned} \tag{9}$$

$$\begin{aligned} G_{\mathrm{TT}}(\omega_r) &= E\left[\int_0^{z_{\max}(x)} [P_U(z(x),\omega_r)^{*} + P_L(z(x),\omega_r)^{*}]\,\mathrm{d}z(x)\int_0^{z_{\max}(x)} [P_U(z(x'),\omega_r) + P_L(z(x),\omega_r)]\,\mathrm{d}z(x')\right] \\ &= \int_0^{z(x)}\int_0^{z(x)}\left[G_{P_UP'_U}(\omega_r,x,x') + G_{P_LP'_L}(\omega_r,x,x') + 2Re(G_{P_UP'_L}(\omega_r,x,x'))\right]\mathrm{d}z(x)\,\mathrm{d}z(x'), \end{aligned} \tag{10}$$

$$\begin{aligned} G_{\mathrm{TN}}(\omega_r) &= E\left[\int_0^{z_{\max}(x)} [P_U(z(x),\omega_r)^{*} + P_L(z(x),\omega_r)^{*}]\,\mathrm{d}z(x)\int_0^{x_{\max}} [P_U(x',\omega_r) - P_L(x',\omega_r)]\,\mathrm{d}x'\right] \\ &= \int_0^{z(x)}\int_0^{x_{\max}}\Big[G_{P_UP'_U}(\omega_r,x,x') - G_{P_LP'_L}(\omega_r,x,x') \\ &\quad + G_{P_UP'_L}(\omega_r,x,x') - G_{P_UP'_L}(\omega_r,x,x')\Big]\,\mathrm{d}z(x)\,\mathrm{d}x', \end{aligned} \tag{11}$$

where $G_{\Delta P\Delta P}$ is given as

$$\begin{aligned} G_{\Delta P\Delta P'}(\omega_r,x,x') &= E[(P_U(x,\omega_r) - P_L(x,\omega_r))^{*}(P_U(x',\omega_r) - P_L(x',\omega_r))] \\ &= E[\Delta P(x,\omega_r)^{*}\Delta P(x',\omega_r)]. \end{aligned} \tag{12}$$

Of course the unsteady pressure measurements are not defined spatially in a continuous manner and, therefore, the above equations must be discretized. The final discretized forms of these equations are

$$G_{\mathrm{NN}}(\omega_r) = \sum_{i=1}^{6}\sum_{j=1}^{6} G_{\Delta P\Delta P}(\omega_r,x_i,x_j)\Delta x_i\Delta x_j, \tag{13}$$

$$G_{\mathrm{TT}}(\omega_r) = \sum_{i=1}^{6}\sum_{j=1}^{6}\left[G_{P_UP_U}(\omega_r, x_i, x_j) + G_{P_LP_L}(\omega_r, x_i, x_j) + 2Re(G_{P_UP_L}(\omega_r, x_i, x_j))\right]\Delta z(x_i)\Delta z(x_j), \tag{14}$$

$$\begin{aligned} G_{\mathrm{TN}}(\omega_r) = \sum_{i=1}^{6}\sum_{j=1}^{6}\big[&G_{P_UP_U}(\omega_r, x_i, x_j) - G_{P_LP_L}(\omega_r, x_i, x_j) \\ &+ G_{P_UP_L}(\omega_r, x_i, x_j) - G_{P_UP_L}(\omega_r, x_i, x_j)\big]\Delta z(x_i)\Delta x_j. \end{aligned} \tag{15}$$

The indices i and j run from 1 to 6 and correspond to the six microphone locations used in the unsteady lift calculation. The formulation of the unsteady lift in this manner raises two important questions which are addressed prior to presenting the calculated lift spectra: (1) what is the effect of the discrete microphone spacing used to form the unsteady lift spectra, and (2) what is the effect of the airfoil to flow-aligned coordinate transformation?

These questions are addressed here.

5.2.1.1. Effects of discrete microphone spacing on lift. The equations used in the unsteady lift formulation are presented above in definite integral form. For practical implementation with a discrete measurement system these equations must be discretized. Consider, e.g. the discretization of the normal-to-chord force spectra G_{NN},

$$\begin{aligned} G_{\mathrm{NN}}(\omega_r) &= \int_0^{x_{\max}}\int_0^{x_{\max}} G_{\Delta P\Delta P'}(\omega_r, x, x')\,\mathrm{d}x\,\mathrm{d}x' \\ &\approx \sum_{i=1}^{6}\sum_{j=1}^{6} G_{\Delta P\Delta P'}(\omega_r, x_i, x_j)\Delta x_i\Delta x_j. \end{aligned} \tag{16}$$

$G_{\Delta P\Delta P}$ is defined only at the microphone measurement locations and therefore must be approximated at all other locations. An error can result from this discrete computation if $G_{\Delta P\Delta P}$ is not adequately defined in rapidly changing regions. In the leading-edge region $G_{\Delta P\Delta P}$ reaches a peak and drops off quickly moving down the chord. This function must be defined with sufficient resolution for the lift computation to be accurate.

A check on spatial resolution adequacy is performed via simulation using Amiet's [50,51] theory. Amiet's theory is used to compute the unsteady pressure at the same chordwise locations used in the experiment from which the unsteady lift can be computed as outlined above. This lift spectrum in then compared to a lift spectrum calculated from Amiet's theory using a continuous distribution of pressure. The continuous unsteady lift spectrum calculation is performed in a quasi-continuous manner by taking a very small Δx's (0.14% chord). The von Karman turbulence spectrum is used in this calculation with the integral scale and turbulence intensity taken as the values in the experiment.

Fig. 10 presents a comparison of lift calculated from predicted continuous and discrete distribution of surface pressure (the angle of attack is zero; i.e. Amiet's solution does not allow for airfoil mean loading). Notice the discrete lift falls below the continuous by 0.7 dB. The decrease of the simulated discrete lift is a consequence of cutting off the pressure peak at the leading edge. That is, consider Fig. 11, a plot of Amiet's $G_{\Delta P\Delta P}$ at $x/c = 2.5\%$ chord for $\omega_r = 10$ as a function of $x/c – x/c'$ (where x/c' is every chordwise position) for both the discrete and continuous case. In the leading-edge region, $G_{\Delta P\Delta P}$ rises up at a high rate as a consequence of the singularity occurring there. This portion of the pressure distribution is not included in the discrete lift calculation causing the overall level to fall below the continuous calculation. Thus, it can be concluded that in the presence of a noise free measurement calculating lift discretely from pressure measurements will result in a slight reduction (<1 dB) of unsteady lift.

5.2.1.2. Effect of airfoil to flow-aligned coordinate transformation. The next item to consider is the effect of the coordinate transformation implemented in the calculation of unsteady lift which rotates from airfoil aligned to flow-aligned coordinates. When calculating unsteady lift, the pressure difference ΔP is taken across

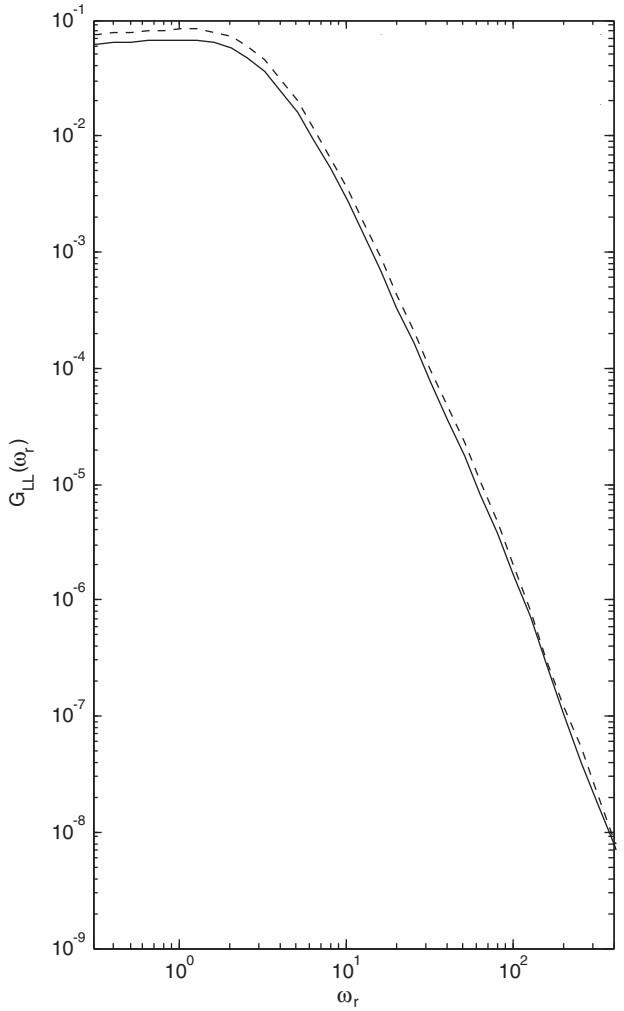

Fig. 10. Calculation of unsteady lift from continuous (……) and discrete (—) distribution of surface pressure. Surface pressure predictions made with Amiet's theory.

the chord (as depicted in Fig. 12(a) and (b)) such that

$$\Delta P(x_1) = P_U(x_1) - P_L(x_1), \tag{17}$$

where $P_U(x_1)$ and $P_L(x_1)$ are the pressure on the upper and lower side of the airfoil, respectively, at chordwise location x_1 in airfoil aligned coordinates. However, it is desired to form the pressure difference in the direction of lift (also shown in Fig. 12(b)) such that

$$\Delta P(x_1^a) = P_U(x_1^a) - P_L(x_1^a), \tag{18}$$

where $P_U(x_1^a)$ and $P_L(x_1^a)$ are the pressure on the upper and lower side of the airfoil, respectively, at location x_1^a in flow-aligned coordinates. Since the actual microphone distribution is fixed and thus, does not allow for pressure differencing in the direction of lift, a coordinate rotation must be implemented to obtain the unsteady lift. This transformation is taken as

$$G_{\mathrm{LL}}(\omega_r) = G_{\mathrm{NN}} \cos^2(\alpha) + G_{\mathrm{TT}} \sin^2(\alpha) - 2Re(G_{\mathrm{TN}}) \sin(\alpha) \cos(\alpha) \tag{19}$$

and is derived above.

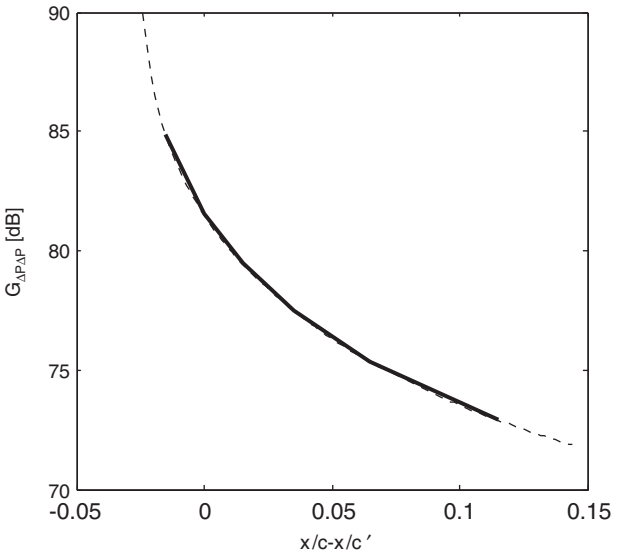

Fig. 11. $G_{\Delta P \Delta P}$ at $x/c = 2.5\%$, $\omega_r = 10$ from Amiet's theory computed continuously (……) and discretely (—), plotted against all other chordwise locations, x/c'.

The effects of this coordinate transformation can be simulated using Amiet's theory. For some angle of attack, α, the actual microphone locations used in the lift calculation (as denoted in Table 6 and Fig. 3) on the top and bottom of the wing are projected into a flow-aligned coordinate system, as shown in Fig. 13. The pressure difference between these projected top and bottom points is then calculated. The lift spectrum, G_{LL} is then computed by numerically integrating these values for each angle of attack and compared with each other. G_{LL} is computed as follows (using the notation of Fig. 13):

$$G_{\mathrm{LL}}(\omega_r) = \sum\sum G_{P(x^a_{nU})P(x^a_{mU})}\Delta x^a_{nU}\Delta x^a_{mU} + \sum\sum G_{P(x^a_{nU})P(x^a_{mL})}\Delta x^a_{nU}\Delta x^a_{mL} + \sum\sum G_{P(x^a_{nL})P(x^a_{mU})}\Delta x^a_{nL}\Delta x^a_{mU} + \sum\sum G_{P(x^a_{nL})P(x^a_{mL})}\Delta x^a_{nL}\Delta x^a_{mL}. \quad (20)$$

Fig. 14 presents unsteady lift calculated in this manner for $\alpha = 0^\circ$, 4°, 8°, 12°, 16°, and 20°. The lift spectra calculated using Amiet's simulation show little variation (<1 dB) as a consequence of the coordinate transformation. Therefore, it is concluded that lift spectra are not significantly affected by the transformation from airfoil to flow-aligned coordinates.

Another perspective on the coordinate transformation can be taken which considers the phasing of the pressure response across the chord. When the airfoil is at angle of attack pressure sensors on the suction side of the airfoil are further away from the stagnation point than their companions on the pressure side. This results in a slight phase difference between the pressures measured on each side of the airfoil, as shown in Fig. 15. The phase difference can be modeled by considering the pressure fluctuations to be harmonic in space and time. Referring to the notation of Fig. 16, the pressure at $\alpha = 0^\circ$ is given as

$$\Delta P(\alpha = 0) = 2P\mathrm{e}^{\mathrm{i}\omega(t+(d_s/U_\infty))} \quad (21)$$

and the pressure at non-zero angle of attack as

$$\Delta P(\alpha) = P\mathrm{e}^{\mathrm{i}\omega(t+((d_s+x_0)/U_\infty))} + P\mathrm{e}^{\mathrm{i}\omega(t+((d_s-x_0)/U_\infty))}. \quad (22)$$

Now, by taking the ratio of Eqs. (21) and (22) the effect of the phasing difference is revealed as

$$\frac{\Delta P(\alpha)}{\Delta P(\alpha = 0)} = \frac{P\mathrm{e}^{\mathrm{i}\omega(t+((d_s+x_0)/U_\infty))} + P\mathrm{e}^{\mathrm{i}\omega(t+((d_s-x_0)/U_\infty))}}{2P\mathrm{e}^{\mathrm{i}\omega(t+(d_s/U_\infty))}} = \cos\left(\frac{\omega x_o}{U_\infty}\right). \quad (23)$$

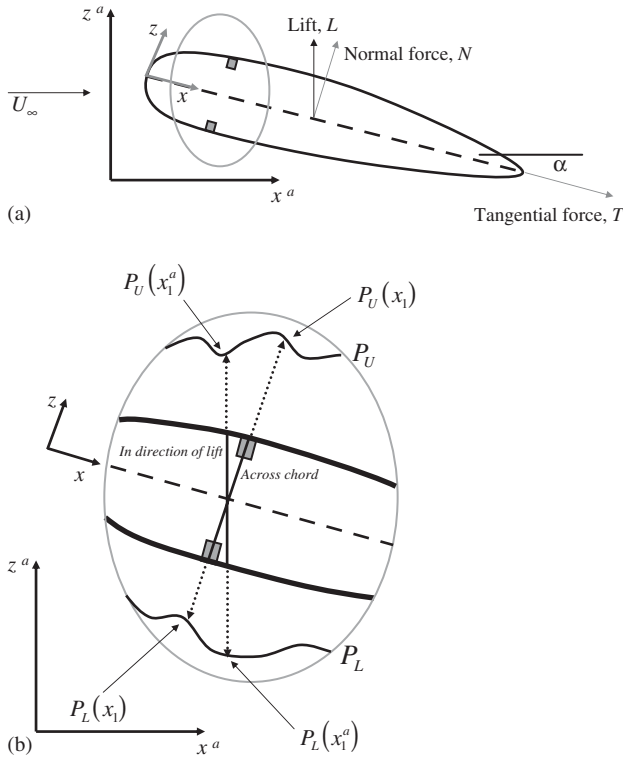

Fig. 12. (a) Depiction of coordinate transformation used to form unsteady lift and (b) close up depiction of coordinate transformation used to form unsteady lift.

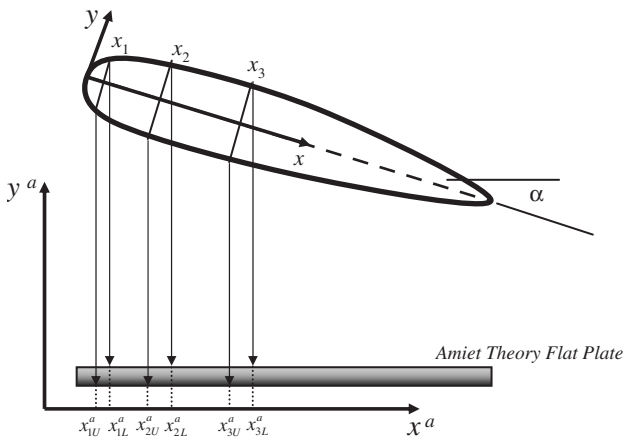

Fig. 13. Projection of microphone locations into flow-aligned coordinate system for Amiet theory simulation.

In forming the power spectral density of pressure fluctuations, the pressure difference is multiplied by its conjugate and, as such, Eq. (23) is squared. If x_0 is assumed constant then integrating along the chord will not affect the result of Eq. (23). A plot of the phase shift model (Eq. (23) squared) as a function of frequency for each angle of attack is presented in Fig. 17. The phase shift model predicts no reduction in unsteady lift for $\omega_r < 10$; however, reduction in unsteady lift above $\omega_r = 10$ is possible based on this model. Therefore, it is concluded that the coordinate rotation associated with forming lift spectra from measured unsteady pressure will not adversely affect this calculation at low reduced frequencies.

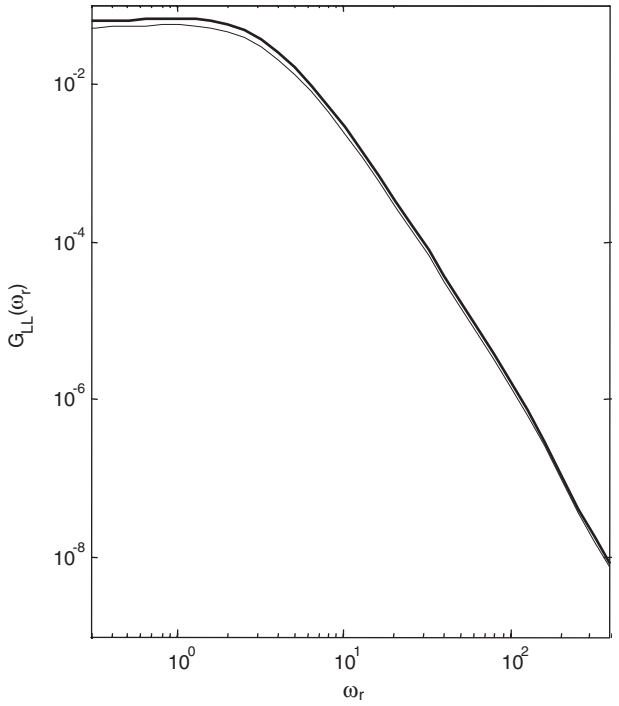

Fig. 14. Lift spectra calculated from Amiet's theory simulating the effects of the coordinate rotation from airfoil to flow-aligned coordinates (▬ ▬, $\alpha = 0°$; – – –, $\alpha = 4°$; — -, $\alpha = 8°$; ▬▬, $\alpha = 12°$; —, $\alpha = 16°$; — -, $\alpha = 20°$).

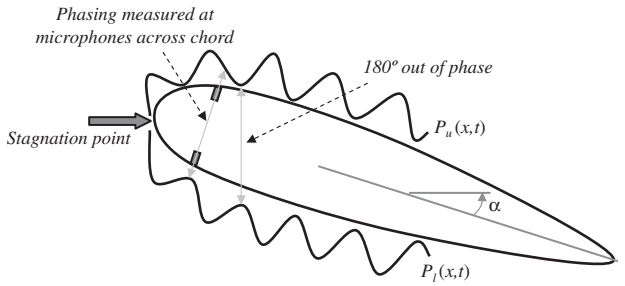

Fig. 15. Drawing showing phase shift in pressure when airfoil is at non-zero angle of attack.

5.2.1.3. Presentation of lift spectra. Having shown above that the formulation used to compute unsteady lift from pressure measurements is valid, the lift spectra G_{LL} are presented here in Fig. 18. These spectra are calculated as outlined above for $\alpha = 0°$, 2°, 4°, 6°, 8°, 10°, 12°, 14°, 16°, 18°, and 20° with spectral level plotted against ω_r and normalized on $(qc)^2$, where q is the dynamic pressure and c the chord. The measured effect of mean loading is very surprising in light of previous mathematical and experimental work on this problem and is consistent with that shown in pressure spectra presented above. Two frequency dependent interaction regions are shown in Fig. 18; at low frequencies ($\omega_r < 5$) a suppression of unsteady lift with increasing angle of attack occurs with a maximum lift reduction of 5 dB occurring between $\alpha = 0°$ and 14°. The opposite effect occurs at high frequencies ($\omega_r > 5$) with a rise in unsteady lift of up to 10 dB occurring with increasing angle of attack. It should be noted that the lift spectrum at $\alpha = 20°$ shows significant unsteadiness at low ω_r which results from large-scale pressure fluctuations associated with stall. Airfoil stall at this angle of attack is corroborated by mean pressure measurements and flow visualization.

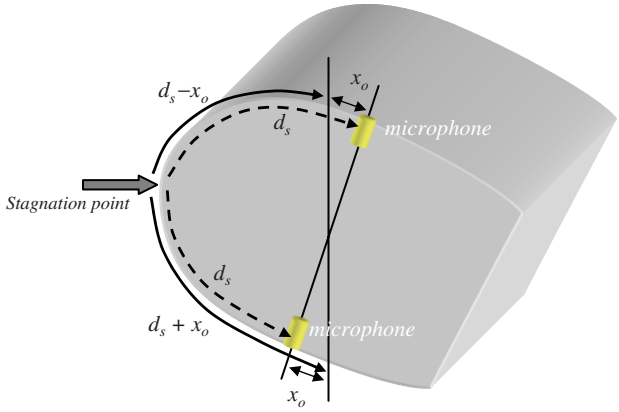

Fig. 16. Drawing of leading-edge region of airfoil showing the nomenclature used in the phasing model.

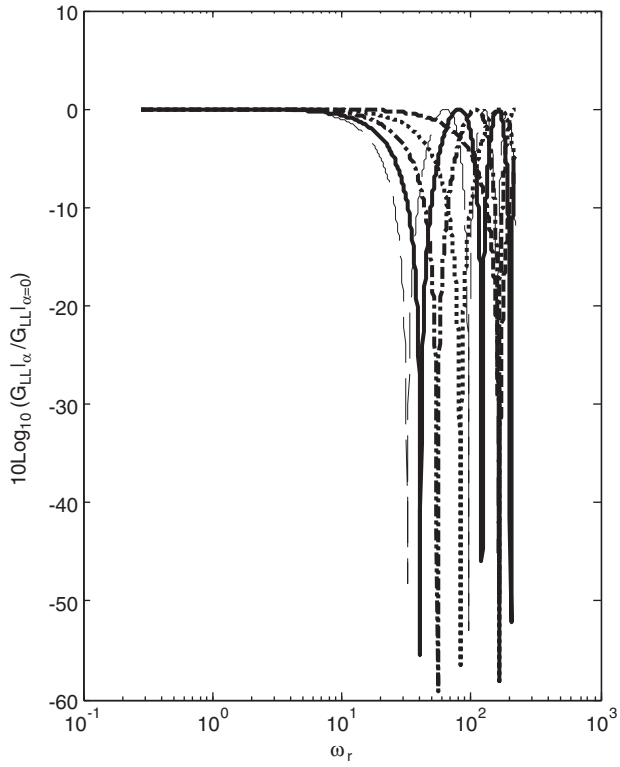

Fig. 17. Predicted reduction in lift as a result of surface pressure phase shift which arises from coordinate rotation during calculation of lift from pressure measurements. Prediction based on phase shift model, square of Eq. (23) (▬ ▬, $\alpha = 0^\circ$; – – –, $\alpha = 4^\circ$; — -, $\alpha = 8^\circ$; ▬▬, $\alpha = 12^\circ$; —, $\alpha = 16^\circ$; — -, $\alpha = 20^\circ$).

The reduction in lift spectral level at low ω_r is a never before measured result and unexpected based on previous experimental and theoretical studies. McKeough [24] showed, through unsteady lift measurements on a NACA 0015 in turbulence, an increase in unsteady lift with an increase from $\alpha = 0^\circ$ to 10°. Paterson and Amiet [44] discussed, although did not present supporting data, an increase in surface pressure spectral magnitude with increasing angle of attack. The present result is also not supported by theoretical formulations which account for airfoil mean loading, such as the theories developed by Reba and Kerschen [52],

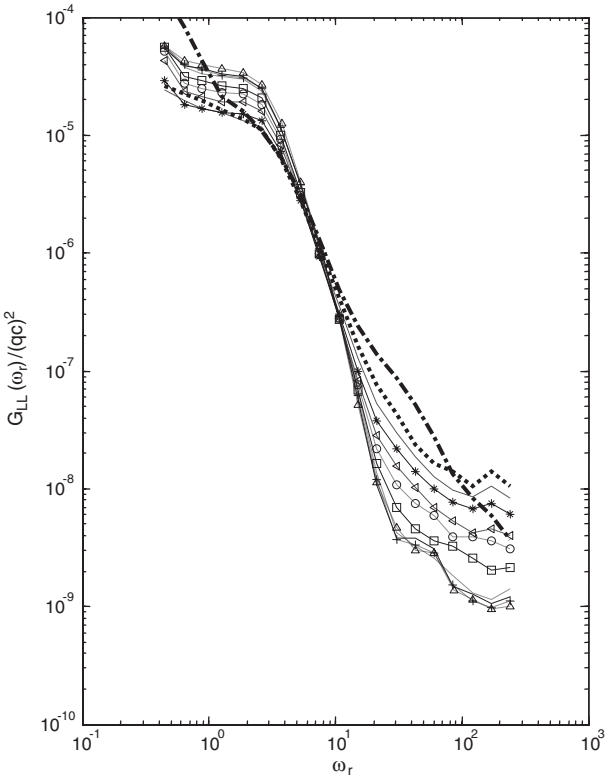

Fig. 18. Unsteady lift calculated from pressure measurements over the first 14% chord (--△--, $\alpha = 0°$; —, $\alpha = 2°$; --+--, $\alpha = 4°$; ……, $\alpha = 6°$; –□–, $\alpha = 8°$; --o--, $\alpha = 10°$; —◁—, $\alpha = 12°$; —*—, $\alpha = 14°$; ———, $\alpha = 16°$; ▪▪▪▪▪▪, $\alpha = 18°$; ▬▪▬▪, $\alpha = 20°$).

Graham [8], and Atassi [26]. In fact, predictions made by McKeough using Graham's [8] theory compare well with the increase in unsteady lift amplitude he measured.

5.2.1.4. Effects of forming the lift over the first 14% chord. The effects of limiting the integration of unsteady pressure to the first six microphones (i.e. up to 14% chord) is examined to ensure the trends with angle of attack are not influenced by this bounding. Lift spectra calculated using all 13 chordwise microphones (integration up to 85% chord) show the same angle of attack observations revealed in spectra formed with the first 14% chord suggesting the 14% chord bounding does not influence the observed angle of attack effects. All subsequent discussions related to lift spectra refer to spectra that are formed by integrating from 0% to 14% of the airfoil chord.

5.2.2. Lift spectrum at zero angle of attack

The $\alpha = 0°$ normalized lift spectrum, $G_{LL}/(qc)^2$ is presented in Fig. 19 along with that calculated from Amiet's [50,51] theory. Over low ω_r (<5) the measurement and prediction are within 1 dB and the agreement in shape is very good. The measured G_{LL} begins to fall off with a greater slope than the predicted for $5<\omega_r<20$. The spectral levels are within 10 dB in this region. The difference in slope of the predicted G_{LL} is likely related to the zero thickness flat-plate model used in this theory. The predicted and measured G_{LL} crossover at $\omega_r = 120$ as a consequence of the change in slope of the measured G_{LL}. The change in slope which occurs at higher ω_r is likely related to turbulent boundary layer pressure fluctuations and eddy convection which become significant at higher frequencies and tend to dominant the unsteady lift over this frequency range.

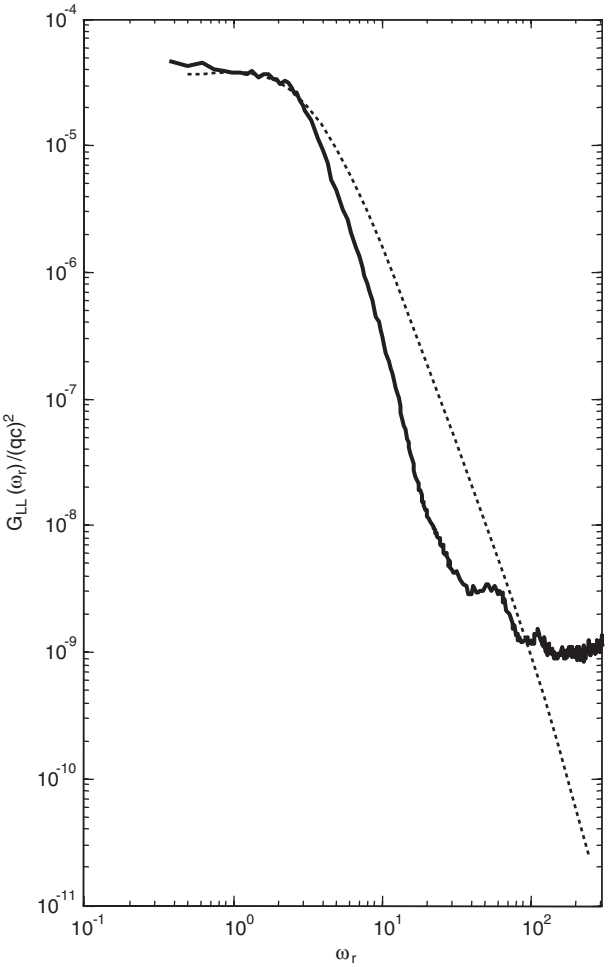

Fig. 19. Comparison of $\alpha = 0^\circ$ lift spectrum calculated from measured pressure (——) with lift spectrum predicted by Amiet's theory (▪▪▪▪▪▪). Both lift calculations are performed by integrating pressure from 0% to 14% chord.

5.2.3. *Lift spectrum at non-zero angle of attack*

The lift spectra calculated from pressure measurements are compared with lift spectra computed from Reba and Kerschen's [52] RDT method in Fig. 20. Lift is calculated for $\alpha = 0^\circ$, 2°, and 6° using Reba and Kerschen's theory with the frequency axis of these predictions shifted by a factor of 10 for clarity. A direct comparison of measured and predicted lift spectral levels is not appropriate given the spanwise wavenumber integration restriction (discussed above); however, a comparison of spectral shape and trends with angle of attack is still of substantial value. For small angles of attack ($\alpha < 6^\circ$), the measured G_{LL} falls less than 1 dB for $\omega_r < 5$ as α is increased. By contrast, the predicted spectral levels show a substantial increase of near 14 dB over a similar range of ω_r. The large increase appears to occur as a consequence of the flat-plate model assumed in the theory. The velocity gradients associated with the leading-edge singularity of a flat plate at some α in inviscid flow are much larger than those of an airfoil with thickness. As such, the inflow is not distorted as it would be when encountering a real airfoil with thickness and rounded leading edge.

The measured lift spectra begin to converge and show no effect of angle of attack over $5 < \omega_r < 10$. The G_{LL} predicted by the Reba and Kerschen method over this ω_r range increases with increasing angle of attack by as much as 6 dB; however, the spectra appear to be converging at higher ω_r. Again, the increase predicted in this frequency range is likely the result of the flat-plate model. For $\omega_r > 10$ the slope of the measured G_{LL} begins to decrease as pressure fluctuations associated with the turbulent boundary layer and convection begin to affect

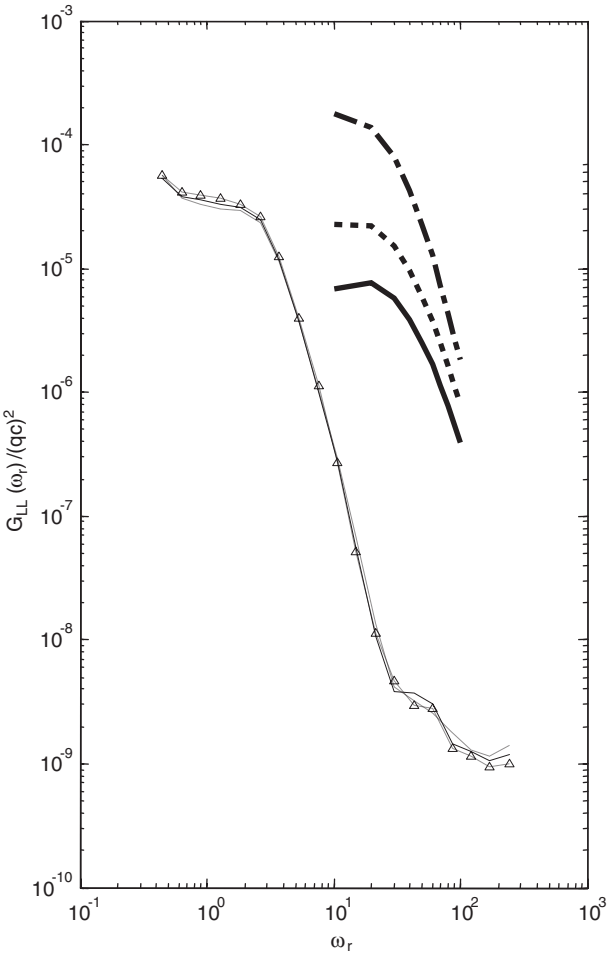

Fig. 20. Comparison of lift spectra calculated from measured pressure (--△--, $\alpha = 0^\circ$; —, $\alpha = 2^\circ$; ▪▪▪▪▪, $\alpha = 6^\circ$) with lift spectra predicted by Reba and Kerschen's theory (▬▬, $\alpha = 0^\circ$; ▪ ▪ ▪, $\alpha = 2^\circ$; ▬ ▪, $\alpha = 6^\circ$). Predictions are shifted by a factor of 10 to the right.

the unsteady lift. Comparisons with Reba and Kerschen's theory were not possible over this frequency range due to difficulties in implementing the complex error-function routine used in their FORTRAN code.

5.2.4. Mean square lift at non-zero angle of attack

The lift spectrum calculated from the first 14% chord is integrated at each angle of attack to obtain $\bar{L}^2$values as

$$\bar{L}^2(\alpha) = \int G_{\mathrm{LL}}(\alpha, f)\,\mathrm{d}f \tag{24}$$

with integration limits of $\omega_r = 0.35-10$. Mean square L values normalized on $(qc)^2$, where q is the dynamic pressure and c the chord, are presented in Fig. 21 as a function of angle of attack. As pointed out by McKeough and Graham [25] and as suggested by the variation in measured pressure and lift spectra levels, angle of attack effects should appear first in terms of order α^2 when the inflow is homogeneous. This implicitly makes sense when one considers that a positive or negative shift in angle of attack away from $\alpha = 0^\circ$ should produce the same effect on the unsteady loading for a homogeneous inflow. Therefore, Fig. 21 also shows a curve representing an α^2 variation in mean square lift for comparison with the data. As the angle of attack is increased the mean square L decreases nearly as α^2 up to $\alpha = 14^\circ$ with the α^2 curve within 6% of the measured

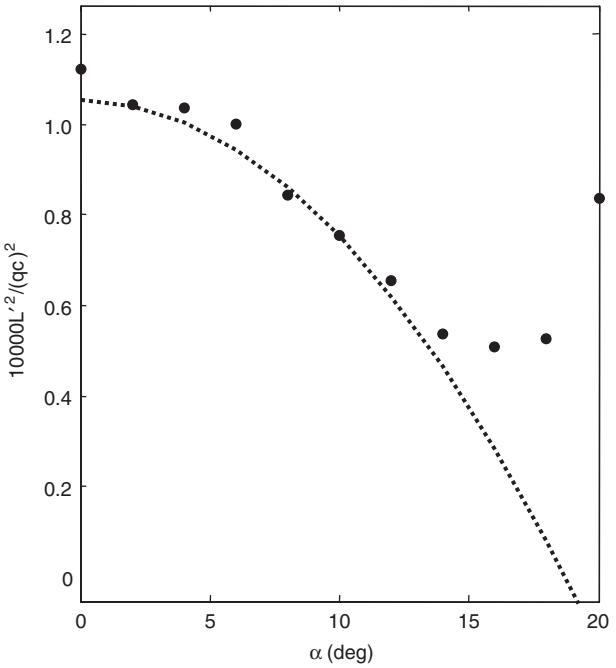

Fig. 21. Measured L'^2 (●) as a function of angle of attack compared with a curve representing α^2 (▪▪▪▪▪▪, $y = A\alpha^2 + B$).

data up to $\alpha = 14^\circ$. The coefficients, A and B are calculated to be -3.01×10^{-3} and 1.11, respectively. Unsteady lift associated with separation becomes significant at $\alpha = 16^\circ$ causing the rate of decrease in $\bar{L}^2$ to fall. At $\alpha = 20^\circ$ the unsteadiness in the lift is due primarily to stall causing an apparent increase in $\bar{L}^2$.

6. Conclusions

This paper is the first in a series of two papers (Parts 1 and 2 [2]) that experimentally investigates mean-loading effects and their sources on the response of an airfoil encountering turbulence. This paper (Part 1) presents the unsteady surface pressure and lift spectra with particular attention paid to the effects of mean loading. Unsteady pressure measurements were made on the surface of a NACA 0015 immersed in grid turbulence ($\lambda/c = 13\%$, $u'/U_\infty = 3.93\%$) for angles of attack $\alpha = 0-20^\circ$. Measured pressure spectra show a reduction of up to 5 dB with increasing angle of attack for reduced frequencies less than 5. This observed mean-loading effect has never before been measured or shown to occur theoretically. For reduced frequencies greater than 5 a significant increase in spectral level is observed. Lift spectra computed from pressure measurements and therefore, inherently containing surface pressure and pressure difference auto- and cross-spectra, show a similar result. Again, no other experiment or prediction has revealed such a reduction in lift spectral level with increasing angle of attack. Furthermore, the reduction in lift spectral level appears to have an α^2 dependence.

Also, for small angles of attack ($\alpha < 8^\circ$), lift spectral levels reduce by less than 1 dB which suggests that Amiet's zero-mean-loading theory may be useful for predicting the airfoil response in this range. Based on comparisons at $\alpha = 0^\circ$, Amiet's [50,51] theory predicts with reasonable accuracy (within 4 dB at low frequency) pressure and lift spectral levels. This theory also successfully predicts the shape of both pressure and lift spectra and the decrease in pressure spectral level moving away from the airfoil leading edge.

Reba and Kerschen's [52] flat plate unsteady loading theory, which accounts for non-zero-mean loading using RDT, predicts large increases in pressure and lift spectral levels not shown to occur in the measurement. The predicted rise in spectral level appears to result from the flat-plate model with leading-edge singularity which does not fully account for the distortion of the inflow.

Acknowledgements

This work would not have been possible were it not for the kind support of Casey Burley and Tom Brooks of NASA Langley under grant NAG-1-2272. Their insight and feedback on the analysis of this substantial data set is also appreciated.

Appendix A. Formulation of pressure cross-spectral density from measured pressure

The first step in producing the *surface pressure* cross-spectral density from measured pressure data is the application of microphone calibrations. This begins by applying the Fourier transform to each microphone voltage time series, v_m, such that

$$v_m(x,y,f) = \int_{-\infty}^{\infty} v_m(x,y,t)\, \mathrm{e}^{-\mathrm{i}2\pi ft}\, \mathrm{d}t, \tag{A.1}$$

which is numerically implemented as

$$v_m(x,y,f_k) = \sum_{j=1}^{N_s} v_m(x,y,t_i)\, \mathrm{e}^{(2\pi \mathrm{i}/N_s)(j-1)(k-1)}, \tag{A.2}$$

where j and k are indices for each time and frequency increment, respectively, and $N_s = 2048$ (i.e. the record length). The microphone calibration, M_s (V/Pa) is applied to each microphone voltage spectrum to obtain pressure, p' (Pa), as

$$p'(x,y,f) = \frac{v_m(x,y,f)}{M_s(m_n,f)}, \tag{A.3}$$

where m_n is a unique number assigned to each microphone. The *surface pressure* cross-spectral density is then formed as

$$S_{qq}(x_i,x_j,\eta,f) = \frac{2}{N_s S_R} E[p'(x_i,y_i,f)^* p'(x_j,y_j,f)], \tag{A.4}$$

where $E[\,]$ is the expected value, * indicates the complex conjugate, S_R is the sampling rate, and $\eta = y' - y$. Also, i and j denote different measurement locations. The factor of two in Eq. (A.4) accounts for the fact that Eq. (A.1) is only evaluated over the positive time domain. The *pressure difference* cross-spectral density is calculated as

$$S^{\Delta}_{qq}(x_i,x_j,\eta,f) = \frac{2}{N_s S_R} E[\Delta P(x_i,y_i,f)\Delta P(x_j,y_j,f)^*], \tag{A.5}$$

where ΔP is the difference between the lower and upper surface pressure measurements:

$$\Delta P(x,y,f) = P_L(x,y,f) - P_U(x,y,f). \tag{A.6}$$

Throughout this work S_{qq} is used in several different forms which are identified here. The *surface pressure* auto-spectrum, G_{pp}, is related to S_{qq} as

$$G_{pp}(x,f) = S_{qq}(x_i,x_i,\eta = 0,f). \tag{A.7}$$

The *pressure difference* auto-spectrum, $G_{\Delta P\Delta P}$, is related to the cross-spectral density as

$$G_{\Delta P\Delta P}(x,f) = S^{\Delta}_{qq}(x_i,x_i,\eta = 0,f). \tag{A.8}$$

References

[1] R.K. Amiet, Acoustic radiation from an airfoil in a turbulent stream, *Journal of Sound and Vibration* 41 (4) (1975) 407–420.

[2] P.F. Mish, W.J. Devenport, An experimental investigation of unsteady surface pressure on an airfoil in turbulence—part 2: sources and prediction of mean loading effects, *Journal of Sound and Vibration* (2003) (under review).

[3] P.F. Mish, An Experimental Investigation of Unsteady Surface Pressure on Single and Multiple Airfoils, Ph.D. Dissertation, Aerospace and Ocean Engineering Department, Virginia Tech, March 2003, Available at: http://scholar.lib.vt.edu/theses/available/etd-03312003-173021/.
[4] T. von Karman, W.R. Sears, Airfoil theory for non-uniform motion, *Journal of the Aeronautical Sciences* 5 (10) (1938) 379–390.
[5] W.R. Sears, Some aspects of non-stationary airfoil theory and its practical application, *Journal of the Aeronautical Sciences* 18 (3) (1941) 104–108.
[6] J.M.R. Graham, Similarity rules for thin airfoils in non-stationary subsonic flows, *Journal of Fluid Mechanics, Part 4* 43 (1970) 753–766.
[7] E. Reissner, On the application of Mathieu functions in the theory of subsonic compressible flow past oscillating airfoils, NACA TN 2363, 1951.
[8] J.M.R. Graham, Lifting surface theory for the problem of an arbitrarily yawed sinusoidal gust incident on a thin airfoil in incompressible flow, *Aeronautical Quarterly* (1970) 182–198.
[9] C. Osborne, Unsteady thin-airfoil theory for subsonic flow, *AIAA Journal* 11 (2) (1973) 205–209.
[10] R.K. Amiet, Compressibility effects in unsteady thin airfoil theory, *AIAA Journal* 12 (2) (1974) 252–255.
[11] J.J. Adamczyk, Passage of a swept airfoil through an oblique gust, *Journal of Aircraft* 11 (5) (1974) 281–287.
[12] J.J. Adamcyzk, R.S. Brand, Scattering of sound by an airfoil of finite span in a compressible stream, *Journal of Sound and Vibration* 25 (1) (1972) 139–156.
[13] R.K. Amiet, Acoustic radiation from an airfoil in a turbulent stream, *Journal of Sound and Vibration* 41 (4) (1975) 407–420.
[14] N.H. Kemp, On the lift and circulation of airfoils in some unsteady-flow problems, *Journal of the Aeronautical Sciences* 19 (1952) 713–714.
[15] M. Landahl, *Unsteady Transonic Flow*, Pergamon Press, New York, 1961 (pp. 27–30).
[16] R. Martinez, A.E. Widnall, Unified aerodynamic-acoustic theory for a thin rectangular wing encountering a gust, *AIAA Journal* 18 (6) (1980) 636–645.
[17] J.M.R. Graham, I. Kullar, Small perturbation expansions in unsteady airfoil theory, *Journal of Fluid Mechanics, Part 2* 83 (1977) 209–224.
[18] W.K. Blake, *Mechanics of Flow Induced Vibrations*, vol. II, Academic Press, New York, 1986 (pp. 735–756).
[19] B.D. Mugridge, Sound radiation from airfoils in turbulent flow, *Journal of Sound and Vibration* 13 (1970) 362–363.
[20] H.W. Liepmann, Extension of the statistical approach to buffeting and gust response of wings of finite span, *Journal of the Aeronautical Sciences* 22 (1955) 197–200.
[21] J.H. Horlock, Fluctuating lift forces on airfoils moving through transverse and chordwise gusts, *Journal of Basic Engineering* 90 (1968) 494–500.
[22] P.C. Morfey, Lift fluctuations associated with unsteady chordwise flow past an airfoil, *ASME Journal of Basic Engineering* 92 (1970) 663–665.
[23] M.E. Goldstein, H. Atassi, A complete second order theory for the unsteady flow about an airfoil due to a periodic gust, *Journal of Fluid Mechanics, Part 4* 74 (1976) 741–765.
[24] P.J. McKeough, Effects of Turbulence on Aerofoils at High Incidence, Ph.D. Dissertation, University of London, 1976.
[25] P.J. McKeough, J.M.R. Graham, The effect of mean loading on the fluctuating loads induced on aerofoils by a turbulent stream, *Aeronautical Quarterly* 31 (1980) 56–69.
[26] H.M. Atassi, Sears problem for a lifting airfoil revisited-new results, *Journal of Fluid Mechanics* 141 (1984) 109–122.
[27] H.M. Atassi, J. Grzedzinski, Unsteady disturbances of streaming motions around bodies, *Journal of Fluid Mechanics* 209 (1989) 385–403.
[28] J.R. Scott, H.M. Atassi, A finite-difference, frequency domain numerical scheme for the solution of the gust response problem, *Journal of Computational Physics* 119 (1995) 75–93.
[29] H.M. Atassi, J. Fang, S. Patrick, Direct calculation of sound radiated from bodies in non-uniform flows, *Journal of Fluids Engineering* 115 (1993) 573–579.
[30] M. Myers, E.J. Kerschen, Influence of incidence angle on sound generation by airfoils interacting with high frequency gusts, *Journal of Fluid Mechanics* 292 (1995) 271–304.
[31] K.C. Hall, J.M. Verdon, Gust response analysis for cascades operating in non-uniform mean flows, *AIAA Journal* 29 (9) (1991) 1463–1471.
[32] H.M. Atassi, M. Dusey, C. Davis, Acoustic radiation from a thin airfoil in non-uniform subsonic flows, *AIAA Journal* 31 (1993) 12–19.
[33] C.B. Lorence, K.C. Hall, Sensitivity analysis of the aeroacoustic response of turbomachinery blade rows, *AIAA Journal* 34 (8) (1996) 1547–1554.
[34] J. Fang, H.M. Atassi, Numerical solutions for unsteady subsonic vortical flows around loaded cascades, *Journal of Turbomachinery* 115 (1993) 810–816.
[35] K.S. Aravamudan, W.L. Harris, Low frequency broadband noise generated by a model rotor, *Journal of the Acoustical Society of America* 66 (2) (1979) 522–533.
[36] N.G. Humbad, W.L. Harris, Model Rotor Low-Frequency Broadband Noise at Moderate Tip Speeds, AIAA Paper 80-1013, 1980.
[37] N.G. Humbad, W.L. Harris, Tip geometry effects on model helicopter rotor low frequency broadband noise, in: *AIAA Seventh Aeroacoustics Conference*, October 5–7, Palo Alto, CA, AIAA-81-2003, 1981.
[38] M. Williams, W.L. Harris, Helicopter rotor broadband noise due to rotor–turbulence interaction, FDRL Report 84-1, Department of Aeronautics and Astronautics, MIT Press, Cambridge, CA, 1984.

[39] G.L. Commerford, F.O. Carta, An exploratory investigation of the unsteady aerodynamic response of a two-dimensional airfoil at high reduced frequency, Report UAR-J182, United Aircraft Research Laboratories, East Hartford, CT, 1970.
[40] S.R. Manwaring, S. Fleeter, Rotor blade unsteady aerodynamic gust response to inlet guide vane wakes, *Journal of Turbomachinery* 115 (1993) 197–206.
[41] G.H. Henderson, S. Fleeter, Forcing function effects on unsteady aerodynamic gust response—part 2: low solidity airfoil response, *Journal of Turbomachinery* 115 (1993) 751–759.
[42] G.H. Henderson, S. Fleeter, Airfoil wake and linear theory gust response including sub and super-resonant flow conditions, *Journal of Propulsion and Power* 9 (6) (1993) 847–857.
[43] G.H. Henderson, S. Fleeter, Vortical gust response of a low solidity vane row including steady loading and dynamic stall effects, *Journal of Turbomachinery* 119 (1997) 482–490.
[44] R.W. Paterson, R.K. Amiet, Acoustic Radiation and Surface Pressure Characteristics of an Airfoil due to Incident Turbulence, NASA CR 2733, 1976.
[45] R.W. Paterson, R.K. Amiet, Acoustic radiation and surface pressure characteristics of an airfoil due to incident turbulence, in: *Third AIAA Aero-Acoustics Conference*, Palo Alto, CA, July 20–23, 1976, AIAA Paper 76-571, 1976.
[46] R. Jackson, J.M.R. Graham, D.J. Maull, The lift on a wing in a turbulent flow, *Aeronautical Quarterly* 24 (1973) 155–166.
[47] J.V. Larssen, W.J. Devenport, Acoustic properties of the Virginia tech stability wind tunnel, Report VPI-AOE-263, AOE Department, Virginia Tech, 1999, Available at: http://www.aoe.vt.edu/aoe/physical/vpi-aoe-263.pdf.
[48] S. Bereketab, H. Wang, P. Mish, W.J. Devenport, The surface pressure response of a NACA 0015 airfoil immersed in grid turbulence: characteristics of the turbulence, vol. 1, Final Report to NASA Langley Under Grant NAG 1-1942, AOE Department, Virginia Tech, 2000.
[49] J.S. Bendat, A.G. Piersol, *Random Data: Analysis and Measurement Procedures*, second ed., Wiley, New York, 1986.
[50] R.K. Amiet, High-frequency thin airfoil theory for subsonic flow, *AIAA Journal* 14 (8) (1976) 1076–1082.
[51] R.K. Amiet, Airfoil response to an incompressible skewed gust of small spanwise wave-number, *AIAA Journal* 14 (4) (1976) 541–542.
[52] R.A. Reba, E.J. Kerschen, Influence of airfoil angle of attack on unsteady pressure distributions due to high-frequency gust interactions, Report to NASA Langley Research Center, 1996.
[53] L.T. Filotas, Response of an infinite wing to an oblique sinusoidal gust, *Basic Aerodynamic Noise Research* (1969) 231–246.
[54] P.F. Mish, Mean Loading and Turbulence Scale Effects on the Surface Pressure Fluctuations Occurring on a NACA 0015 Airfoil Immersed in Grid Generated Turbulence, Masters Thesis, Aerospace and Ocean Engineering Department, Virginia Tech, Blacksburg, VA, 2001.
[55] J.J. Bertin, M.L. Smith, *Aerodynamics for Engineers*, second ed., Prentice-Hall, Englewood Cliffs, NJ, 1989 (p. 211).
[56] E.J. Kerschen, M.R. Myers, Incident angle effects on convected gust airfoil noise, in: *AIAA Eighth Aeroacoustics Conference*, April 11–13, Atlanta, GA, AIAA-83-0765, 1983.
[57] J.L. Gershfeld, Leading edge noise from thick foils in turbulent flows, *Journal of the Acoustical Society of America* 116 (3) (2004) 1416–1426.
[58] J.L. Gershfeld, Private communication, March 2002.